MASTER

The design of a tunable diode laser absorption spectroscopy setup for measuring salt additives in metal-halide lamps in micro-gravity

van den Akker, D.

Award date:
2004

The Design of a Tunable Diode Laser Absorption Spectroscopy Setup for Measuring Salt Additives in Metal-Halide Lamps in Micro-Gravity

Danny van den Akker
July 2003
EPG 04-05

Supervisors: Prof. Dr. Ir. G.M.W. Kroesen (Eindhoven University of technology)
Dr. Ir. M. Haverlag (Philips Central Development Lamps)

Summary

In April 2004 the Dutch astronaut Andre Kuipers will fly to the international space station on an ESA mission. During the mission several Dutch research projects will be present and operated by Kuipers. One of the projects is the result from the cooperation between Philips Central Development Lamps and Eindhoven University of Technology. Within this project radial segregation and helical instabilities in High Intensity Discharges lamps will be studied under micro gravity conditions. For this purpose a test setup with 3 diagnostics was built. One of the diagnostics is based on diode laser absorption spectroscopy. In this thesis the development and modifications to perform absorption spectroscopy in burning HID-lamps and the resulting setup are described.

To perform laser absorption spectroscopy in 2 types of thin quartz burners special optical system were designed to correct for the lens working of the quartz burners and perform lateral resolved measurements without any moving parts. To measure at 32 lateral positions a detector head with photodiode array and an on board lock-in amplifier was built and a laser sheet was utilised to illuminate over the full burner diameter.

The external cavity tunable diode laser system that resulted from a survey of available systems, was adapted and built into the setup and successfully tested in the 34th parabolic flight campaign of ESA. The results show that the system is capable of operating in micro gravity and hyper gravity and that absorption experiments can be performed in burning High Intensity Discharge Lamps.

With the system a mode hop free scanning range of 0.071 nm is achievable by coupling the current with the Piezo modulation signal and with coarse tuning of the cavity three salt additives, i.e. Dysprosium, Scandium and Cerium can be measured.

Differences in line width of the absorption line profiles between the burner designs were observed. It is shown that pressure broadening is the main source for line broadening and that the difference of a factor of two in line widths can be explained by assuming a contracted temperature profile. Due to the broader line profiles accurate measurements of the profile wings were not possible and only trends of the mixing and demixing effects could be visualized.

Time resolved measurements show that 20 seconds of micro gravity is insufficient for the lamps to stabilize.

Table of contents

1

Introduction

In April 2004[1] the Dutch astronaut Andre Kuipers will participate in an ESA space mission to the international space station (ISS). On this mission there will be room for several scientific research projects. One of these projects is the result of the cooperation between Eindhoven University of Technology (TU/e) and Philips Central Development Lamps (Philips-CDL). The goal of the project is to design and build a setup in which a set of High-Intensity-Discharge-lamps, shortly HID-lamps, can be studied in zero gravity conditions in the ISS.

HID-lamps are a relatively new product and produced in a multitude of types by Philips and others. HID-lamps are a promising product because of the high efficiency and the amount of light that can be produced in a relatively small volume. The efficiency of the lamps can be up to 40 percent, which is 10 times better than the efficiency of a regular light bulb. Considering the fact that tens of percents of the yearly consumed electrical power is used for lighting, these lamps can have a significant effect on the power consumption.

These lamps are not only interesting from an environmental point of view but also from an application point of view because many applications ask for high light outputs from a small volume. For example in projection and imaging applications like beamers how well the beams are defined determines the quality of the output. Ideally one would like to create a point source to create a very well defined source. The characteristics of the lamps make that they are already used successfully in various applications, like road, stadium, shop and building lighting.

The drawback is that like every new type of product, HID-lamps have some technological problems that are related to the physics of the plasma discharge. It has been observed by various people [2][4][18], this type of lamp shows interesting and new phenomena under certain burning conditions. Two of these phenomena that will be studied during the space mission of Andre Kuipers are de-mixing and helical instabilities of the plasma arc.

De-mixing causes the lamps to burn inhomogeneously and results in a difference in the colour from light generate in the lower part of the burner and light generated in the upper part of the burner.

In a vertical burning position the plasma discharge can become unstable and starts spiralling around the central axis, for the consumer this is seen as a flashing and obviously unwanted effect. It is thought that these helical instabilities occur due to the self generated magnetic fields in the plasma arc, but no real evidence has been found that supports this theory.

Both effects have been and still are studied by several research groups all over the world. The various processes involved are understood quantavely very well [1][2]. To improve the characteristics of HID-lamps in the future and to create an understanding of the underlying processes that cause the problems, experiments and models are needed. The reason that the

---

[1] At the time of writing the space flight of the Dutch ESA astronaut Andre Kuipers that was planned for the end of October 2003 had recently been postponed to April 2004 due to the crash of the NASA space shuttle.

lamps will be studied in zero gravity conditions is that gravity forces on earth induce convective flows in the lamps in such way that the various components in the discharge are effectively mixed and only data of the mixed particle distributions can be obtained. The modelling of the underlying processes therefore has to be performed 3 dimensional, which is not yet possible.

One of the two aims of the space mission is to determine radial density profiles of various salt additives in HID-lamps under various conditions. The profiles will be obtained from two spectroscopic techniques; one based on absorption- and one based on emission-spectroscopy. In this thesis, the design and used method of the absorption part of the setup will be presented, as well as some promising preliminary results obtained during the 34th ESA parabolic flight campaign.

1.1 An introduction to HID-lamps

High Intensity Discharge lamps generate light with a discharge (plasma), similar to a regular tubular fluorescent lamp. The discharge is contained inside a ceramic container called the burner. Figure 1.1 shows an example of a HID-lamp. The burner has a length of around 20 mm and a radius of around 2 mm.

The centre of the discharge has a very high temperature and is typically around 5500 K. The wall temperature of the burner is typically 1200 K. An outer balloon called the BuBa (from BuitenBAllon) encloses the burner for protection and UV shielding. The space around the burner is either vacuum or filled with an inert gas like nitrogen.

The burner is filled with a few milligrams of mercury and salt additives. During operation the mercury evaporates completely and the pressure in the burner increases to several tens of bars, typically between 10-50 bars. The salt additives are often a mixture of sodium-iodide and other metal-iodides.

When the temperature becomes high enough the iodides start to evaporate, dissociate in the discharge and start emitting light. The salts do not evaporate completely, the partial pressure of the additives lies between 5-50 mBar. Therefore the gas in the burner mainly consists of mercury vapour.

Figure 1.1 A typical HID-Lamp

Although mercury vapour determines the pressure of the gas, the salt additives produce most of the light output. By changing the salt-additives the light output is changed and various tones of light can be produced.

The lamps operate on a square wave voltage with a frequency of 400 Hz and cannot be plugged directly in the electricity net. Also the ignition voltage of the lamps is very high. Therefore the lamps are started and operated by an electronic power supply unit called a ballast. The unit ignites the lamps with voltage pulses of 6 kV. After ignition the lamp voltage drops to typically between 70-120 V and via the current running through the lamp the power is regulated by the electronics.

1.2 The influence of gravity forces: segregation and de-mixing

When HID lamps are operated vertically, gravity forces induce convective flows in the plasma. Figure 1.2-B shows the flows schematically. In the hot centre of the discharge the flow is directed upward and at the cooler burner walls downward. The salt is evaporated and the molecules are dissociated in the centre of the discharge into atoms. Therefore a difference exists in the density of molecules and atoms and ions between centre and walls, which results in diffusive flows of molecules to and ions and atoms from the centre of the discharge. This process is radial segregation. Due to differences in diffusion coefficients of the various atoms and ions the radial segregation is different for each of the species, therefore species from the centre with higher diffusion coefficients get further into the convective flows.
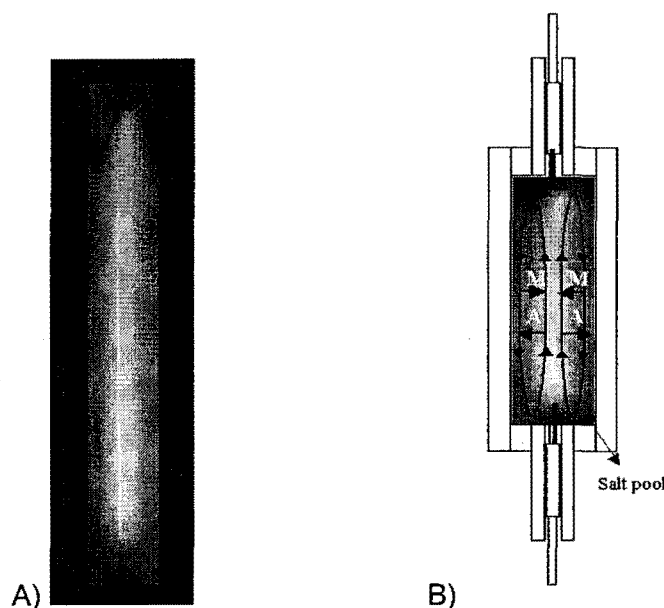
Figure 1.2 A) Schematic of the convective flows and radial segregration B) Axial de-mixing results in a colour gradient, picture taken of a real lamp.the convective flow.

Therefore the particles with lower diffusion coefficients are effectively taken upward by the convective flow and the particles with higher diffusion coefficients downward. The result is an axial demixed discharge, which is visible as a colour gradient over the axis.

To study the radial de-mixing without the disturbing effect of the convection flow there is only one option: switch off gravity. A possible option would be to participate in the ESA parabolic flight campaigns where for a period of 20 seconds micro gravity is obtained with a falling airplane. But the time needed to get to a stable situation in the lamps is much longer than 20 seconds and thus is to short to obtain data of radial segregation without disturbances from the convective flows in the parabolic flights. Therefore the measurements will also be done in the ISS. Although the parabolic flights will not be useful in measuring radial de-mixing, they give the project an opportunity to test the setup in micro-gravity and measure the influence of gravity on the de-mixing effects. Also the amount of salt additive and mercury for

which the radial segregation can be observed the best can be selected from these measurements.

1.3 Measurement of atomic densities

Atomic spectroscopy is the oldest instrumental elemental analysis principle. Kirchoff and Bunsen discovered in the mid 19th century that the optical radiation from flames was characteristic for the elements introduced in it [5]. It was also known at that time that the intensity of the atomic lines increased when more of the same element was added. It shows that at the time atomic emission spectroscopy already was an analytical method to retrieve species information both qualitative and quantitative. In the same period it was found that radiation of the same wavelength as the emission lines could be absorbed by the same gas. This was the basis for atomic absorption spectroscopy.

In the past, researchers have developed a lot of diagnostic methods based on spectrometry to obtain plasma parameters. The problem with obtaining information from inside a plasma is that it is a complex and hot gas and introducing measuring equipment directly in the plasma changes the conditions in the plasma. Therefore many spectroscopic diagnostic methods have been developed to measure various plasma parameters like particle density and temperature, electric- and magnetic fields and gas temperature without disturbing the plasma. One can think of Raman- and, Thomson-scattering, Laser Induced Fluorescence (LIF), Cavity ringdown-, emission- and absorption spectroscopy.

1.4 Diode laser absorption

In absorption spectroscopy the amount of absorbed radiation is directly proportional to the amount of absorbing particles in the path of the radiation. By selecting a resonant atomic transition it is possible to obtain the density of the ground state, which is not possible with emission spectroscopy. Therefore absorption spectroscopy is often used to study neutrals in gas discharges.

A relatively new method in performing absorption spectroscopy is with diode lasers. Diode laser absorption spectroscopy is now a widely used technique in many different applications and environments. Since diode lasers are a relatively cheap and a small type of laser, they are very well suited for applications which demand small size and weight. Examples of applications in which this is needed are gas monitoring and detection systems [3]. Their small size and weight also make diode laser absorption spectroscopy a good candidate for operating in the space mission, since space equipment need to be small and light due to the high uplift costs of Eur 30.000 per kilogram. In this thesis the possibilities of a laser diode based absorption system will be explored and the design of a tunable diode laser absorption setup that resulted from it is described. Also the first test results in micro-gravity conditions

during parabolic flights will be shown. The aim of this thesis is not only to describe the results of the system, but also show the design considerations and the possible application of tuneable diode laser absorption as a diagnostic method in the study of HID-lamps.

2 Theory

In this chapter the principles of absorption spectroscopy and the various line broadening mechanisms that occur in high-pressure discharges will be described. Furthermore the basics of two Abel-inversion methods will be covered that can be used to reconstruct radial profiles from lateral measurements.

2.1 Lambert-Beer law

To describe the absorption of light by a gas or fluid we consider radiation with frequency v and intensity I incident on a volume of gas as depicted in figure 2.1.
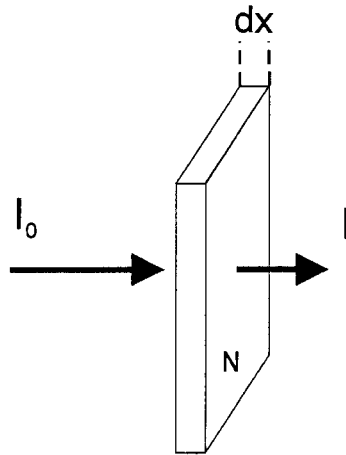
Figure 2.1 schematic for derivation of the Lambert-Beer law

When monochromatic radiation passes through the absorbing medium, the intensity of the incoming light decreases over distance dx by [4]:

$$dI_v(x) = -\alpha_v I_v(x)dx \tag{2.1}$$

With I the incident radiation and $\alpha(v)$ the absorbance of the absorbing medium defined as the integral over the line of sight with length l:

$$\alpha(v) = \int_0^l SN\Phi(v)dx \tag{2.2}$$

Where S is the spectral line intensity and N the number density of the absorbing species. $\phi(v)$ is the lineshape function and represents the probability of finding absorbing events between

frequency ν and ν+dν, figure 2.2 depicts the frequency distribution of a pressure broadening dominated Lorentzian line shape function.
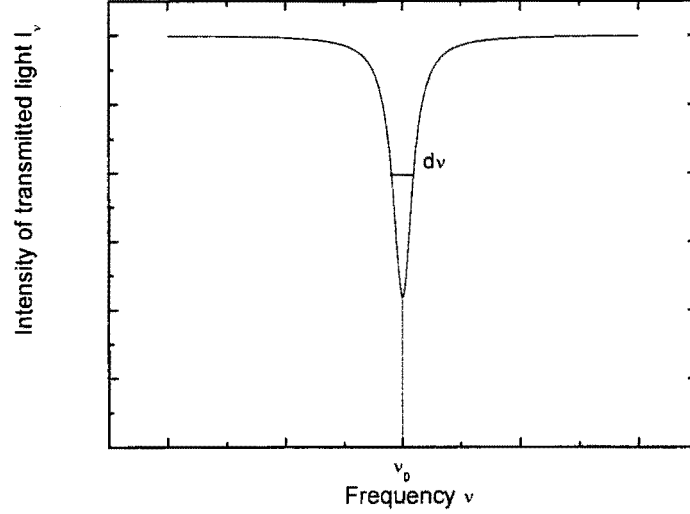
Figure 2.2 An absorption line with a Lorentzian lineshape function

The function is normalised:

$$\int_{0}^{\infty} \phi(\upsilon)d\upsilon \equiv 1 \tag{2.3}$$

Integration of equation 2.1 over an absorbing length l yields the intensity distribution (Lambert-Beer) through the absorbing medium [4]:

$$I_{v}(x) = I_{v}(0)e^{-\int_{0}^{l}\alpha_{v}dx} \tag{2.4}$$

When the absorbing lines are optically thin the absorption over the line of sight l is small and the Lambert-Beer law can be approximated with:

$$I_{v}(x) = I_{v}(0)(1 - \int_{0}^{l}\alpha_{v}dx) \tag{2.5}$$

2.2 Absorption of radiation by atoms

When monochromatic light is guided trough a medium with absorbing species, like a plasma or gas, light can be absorbed by the species if the light matches the energy that is needed to raise the species from the normal state l to the excited state k, according to equation 2.6.

$$\Delta E = E_k - E_i = h\nu \qquad (2.6)$$

The light transmitted trough the species contains the remaining part of the incident light and light emitted by the species. Therefore in the description of absorption spectroscopy all processes must be taken into account. Figure 2.3 depicts the 3 processes at hand; absorption, emission and stimulated emission of radiation.
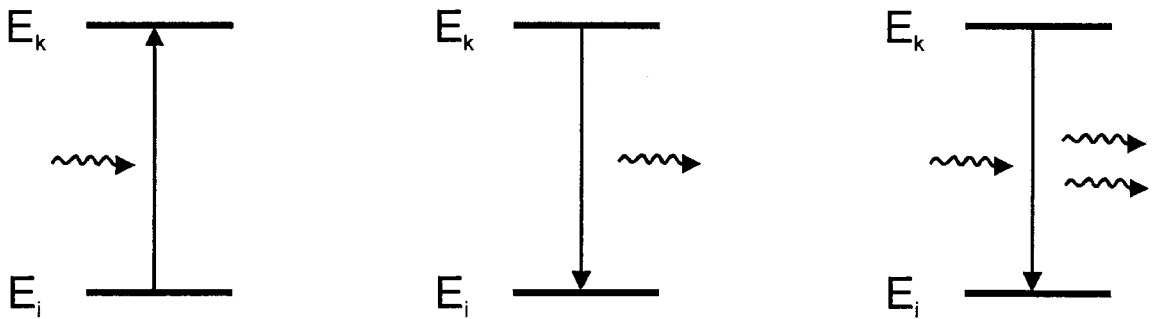
A) Absorption   B) Emission   C) Stimulated Emission

Figure 2.3 The transition processes needed to describe absorption in a light emitting species

The amount of photons that will be absorbed by the species is not only dependent on the amount of particles capable of being raised from the lower energy state I to the higher state k, but also on the probability factors described by Einstein. The Einstein-coefficients for absorption B_{ik}, emission A_{ki} and stimulated emission B_{ki} give the probability per second that an atom exposed to radiation with frequency ν en $\nu+d\nu$ and intensity I will undergo a transition. The number of transitions per second per cm^3 for these processes are proportional to $N_i B_{ik} I(\nu)$, $N_k B_{ki} I(\nu)$ and $N_k A_{ki}$ respectively.

In thermal equilibrium the spontaneous and induced emission equal the absorption: $N_k B_{ki}$ + $N_k A_{ki} = N_i B_{ik}$. Using the Boltzmann distribution of the particles over the energy levels and solving for the spectral energy distribution results in:

$$I(\nu) = \frac{A_{ki} / B_{ki}}{\frac{g_i}{g_k} \frac{B_{ik}}{B_{ki}} e^{h\nu/kT} - 1} \qquad (2.7)$$

Because this is a general equation derived for thermal equilibrium, the emission should follow the Planck distribution. Equating with the Planck distribution results in two expressions for the Einstein coefficients:

$$g_i B_{ik} = g_k B_{ki}, \text{ and } \quad {}_{ki} = \frac{g_i}{g_k} \frac{8\pi h}{c^3} B_{ik} \qquad (2.8)$$

Where g_i and g_k are the statistical weigth factors of the corresponding energy levels and are related to the quantum number J by g=2J+1. With these equations the correlation between the various processes in thermal equilibrium has been established.

When radiation matching a transition of a species, e.g. laser light with the right frequency, is guided through a plasma a portion of that light is absorbed in the plasma. At the same time light is created by stimulated emission and since these photons have the same direction and phase as the source photons they will follow the path of the incoming beam. Therefore the measured absorption coefficient on the detector is a combination of the transmitted light, light emitted by the plasma and the light from the process of stimulated emission. It is often assumed that because the emitted light from the plasma is directed in all directions and of much lower spectral intensity than the probing light and therefore can be neglected. To give a complete picture, the emission is included in the description.

From the Einstein coefficient for induced emission we know that the amount transitions per second due to absorption in the slab is given by $I(v)N_iB_{ik}$. Each transition removes energy hv_0 from the incident radiation. But stimulated emission of radiation adds energy to the incident beam, resulting in an addition of $I(v)N_kB_{ki}$ transitions per second. In which every transition adds energy hv_0. Again from the situation depicted in figure 2.1 the energy absorbed per unit of time is then given by:

$$d[I_v \delta v] = -\frac{I_v}{4\pi}\left(B_{ik}\delta N_i - B_{ki}\delta N_k\right)hvdx \qquad (2.9)$$

With $\dfrac{I_v}{4\pi}$ the intensity of the equivalent isotropic radiation for which B_{ik} and B_{ki} are defined.

Rewriting 2.9:

$$\frac{1}{I_v}\frac{dI_v}{dx}\delta v = -\frac{hv}{4\pi}(B_{ik}N_i - B_{ki}N_k) \qquad (2.10)$$

Using equation 2.1:

$$\alpha(v)\delta v = \frac{hv}{4\pi}(B_{ik}\delta N_i - B_{ki}\delta N_k) \qquad (2.11)$$

Integration over the line profile yields:

$$\int_{Line} \alpha(\upsilon) d\nu = \frac{h\nu_0}{c} \left(B_{ik} N_i - B_{ki} N_k \right) \tag{2.12}$$

Using the equations in 2.8,

$$\int_{Line} \alpha(\upsilon) d\nu = \frac{h\nu_0}{c} N_i B_{ik} \left(1 - \frac{g_i}{g_k} \frac{N_k}{N_i} \right) \tag{2.13}$$

With these equations the density of the lower state can be calculated from measurements of the absorption profile integrated absorption and known transition probabilities. The detailed balancing used to derive the equation is initially based on thermal equilibrium (TE) assumptions; if this approach is generalized it also holds in non-TE conditions.

Often not the Einstein coefficient for absorption is given but the absorption oscillator strength f. f follows from the classical electron theory of dispersion and is defined as [6]:

$$\int \alpha(\upsilon) d\upsilon = \frac{\pi e^2}{mc} N_i f \tag{2.13}$$

Values for transition probabilities and oscillator strength can be found for many species in the Kurucz and NIST spectroscopic databases [7], [8].

2.3 Line broadening of atomic absorption lines

As mentioned before the absorption profile of an atomic transition is a profile that exists over a certain frequency range due to line broadening by particle-particle interactions and the movement of the atoms in the discharge. In this section the profiles and the widths of natural broadening, Doppler broadening and pressure broadening will be described.

Natural broadening

Absorption of radiation occurs between two distinct energy levels of an atom. Heisenbergs uncertainty principle $\Delta E \cdot \Delta \tau \sim h$ states that the energy spread in the atomic level is dependent on the mean lifetime τ of the state. An expression for the classical mean lifetime can be calculated from considering a damped classical oscillator, which results in a lorentzian profile with a FWHM (Full Width at Half Maximum as depicted in figure 2.2) $2\gamma/4\pi = 1/2\pi\tau_{class}$ and is given by [4]:

$$I(v) = I_0 \frac{(\gamma/4\pi)^2}{(v-v_0)^2 + (\gamma/4\pi)^2} \text{ with } \tau_{class} = \frac{3\varepsilon_0 mc^3}{2\pi e^2 v_0^2} \tag{2.14}$$

Doppler broadening

Due to the thermal motion of the particles in the discharge, the absorption line is broadened by the well-known Doppler effect. The Doppler effect causes a shift in the frequency of the radiation absorbed by a particle moving either towards or away from the position of the observer. A particle moving in the direction of the laser beam absorbs light with a frequency higher than the frequency expected from the atomic transition (blue shift) and a particle moving in the opposite direction can absorb at a lower frequency (red shift) than is calculated from the transition. In the case of a Maxwellian velocity distribution, the resulting line profile is a Gaussian profile [4]:

$$I_v = I_0 e^{-c^2(v_0-v)^2/v_0^2\alpha^2} \tag{2.15}$$

The width of the profile is determined by α, 'the most probable velocity' of the velocity distribution and is given by:

$$\delta v_D = \frac{2v_0\alpha}{c}\sqrt{\ln 2} = \frac{2v_0}{c}\sqrt{\frac{2RT\ln 2}{M}} = 7.16 \cdot 10^{-7} v_0 \sqrt{\frac{T}{M}} \tag{2.16}$$

With v_0 the centre frequency of the absorption profile, T the temperature and M the mass number of the absorbing species.

Pressure broadening

Another form of broadening occurs by perturbations of neighbouring particles, i.e. particle-particle interactions. The type of pressure broadening is characterized by the particle that induces the broadening. Stark-broadening is caused by free electrons, resonance broadening by particles of the same species and Van Der Waals broadening by other species.

Resonance broadening:

$$\Delta v_R \approx 8.6 \cdot 10^{-30} \sqrt{(g_i/g_k)} v^2 v_r f_r N_i \tag{2.17}$$

van der waals broadening

19

$$\Delta v \approx 3.0 \cdot 10^{16} \, v^2 C_6^{2/5} (T/\mu)^{3/10} N \qquad (2.18)$$

Where μ is the reduced mass of the perturber atom in U, N the perturber density and C_6 the interaction constant for Van Der Waals broadening.

2.4 Abel inversion technique

In many spectroscopic measurements the cylindrical symmetry of the system under investigation is exploited by using the Abel inversion technique to reconstruct a radial-profile from a lateral measured profile. This makes it possible to measure through a discharge and still obtain radial information.
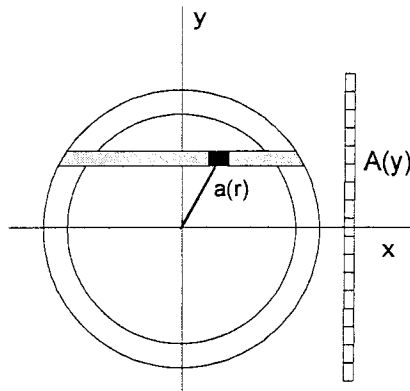
Figure 2.4 Geometrical situation used in Abel inversion

From the geometry depicted in figure 2.4 it can be deducted that for the measured lateral absorption it holds [9]:

$$A(y,\lambda) = \int_{-\infty}^{\infty} a(x,y,\lambda)dx = 2 \int_0^{\infty} a(x,y,\lambda)dx \qquad (2.19)$$

Considering that $a(x,y,\lambda)$ can be written as a function of r, by assuming cylindrical symmetry, the equation becomes:

$$A(y,\lambda) = 2 \int_{r=y}^{\infty} \frac{a(r,\lambda)r}{\sqrt{r^2 - y^2}} dr \qquad (2.20)$$

From the lateral measured profile the radial profile can be reconstructed by numerically solving the following integral:

$$a(r) = -\frac{1}{\pi} \int_r^\infty \frac{I'(y)}{\sqrt{r^2 - x^2}} dy \qquad\qquad (2.21)$$

Abel inversion is known to be very sensitive for errors and since the measured values at the edges determine the solved values in the middle, Abel inversion is very error sensitive in the center of the lateral profile. In our study the profiles are expected to be hollow, making it even worse.

A possible direct approach to reconstruct the radial profiles is by assuming a radial profile with the same amount of points as the measured lateral profile has from the centre to the edge of the lamp. By calculating the corresponding lateral values with equation 2.20 and using a least-square method on the calculated and the measured data and a numerical procedure that adjusts the assumed radial values by minimizing the least-square results, the radial profile can be found [10].

To reduce the error sensitivity of the procedure, the radial profile can be approximated by a polynomial function:

$$a(r) = \sum_0^n c_n r^n \qquad\qquad (2.22)$$

Again with equation 2.20 the lateral values can be calculated, by substituting equation 2.22 in equation 2.20. The coefficients resulting from the integration for the different terms of equation 2.22 are given in appendix A. By using a fit procedure on the measured data and the coefficients c_n of the nth-order polynomial as fit parameters the Abel inversion results can be improved for data with noise on it.

It must be noted that when the line width of the absorption profile varies with radial position that the Abel inversion cannot be used on the integrated absorption profiles, i.e the lateral absorbance. This makes direct Abel inversion of the lateral measured absorption for density profiling invalid and the absorption profile must be reconstructed as a function of the radial position by Abel-inverting for all wavelengths separately.

From the radially reconstructed profiles, the radial absorbance can be determined, from which the density can be deduced. Because the line width of the profiles is broader near the walls than in the centre part of the discharge, the smaller lines are lost in the integrated lateral signal. To reconstruct the thinner lines in the centre with Abel inversion minor differences in the line width of the lateral signal must be measurable and together with the fact that the Abel inversion technique very error sensitive in the centre part, the quality of the measurements must be very high.

3 Tunable Diode Lasers

3.1 Introduction

Since the first semi-conductor laser was developed in 1962 by Gunther Fenner [9], the area of application of laser diodes has grown tremendously. Mainly the telecommunication market and the CD-player and the bar-code reader have pushed the development of the laser diode. Besides the main applications laser diodes have proven their use in research and science and today their application area is still growing fast. Diode lasers are often used in high-resolution spectroscopy and particle sensing applications and recent development of high power laser diodes and diode arrays have resulted in new diode laser pumped systems with a variety of output wavelengths. The high efficiency, spectral properties and compactness make the laser diode a candidate for operation in a new area of application; research in the international space station. In this section the various types of laser diodes, their spectral characteristics, tunability and usage in absorption spectroscopy will be described.

3.2 Index and gain guided laser diodes

All laser diodes are based on the principle of charge carrier recombination between the conduction and valence band in semi-conductor materials. When the charge-carriers recombine photons can be created with an energy that corresponds to the energy difference between the valence band and the conduction band of the materials.

In intrinsic semi-conductor material the valence band is filled with electrons, the conduction band is empty because the Fermi level is situated in the band gap of the material. This makes that the material is non-conductive. By adding electron donor material, or electron acceptor (hole donor) material n and p-doted material is created. In these materials the Fermi-level shifts to just inside the conduction band or valence band and therefore the materials become conductive. By combining n-doted and p-doted material in a junction, the electrons in the conduction band can recombine with the holes in the valence band. In this way, photons can be created.

To create a semi-conductor with a certain wavelength output, a semi-conductor material with a band gap corresponding to the wavelength to produce is needed. For instance, AlGaAs can emit between 780-880 nm and GaInP between 670-680 nm. Although these diodes emit light, they are not laser diodes because they emit over a broad range of wavelengths and the light is not polarized.

To get laser working, an optical resonator and population inversion are required to have amplification and stimulated emission. It can be shown that the population inversion is achieved at a definite current trough the material [11]. To create the optical resonator the

facets of the first hetero-junction diode lasers were cut along crystal planes and had a reflectivity of around 32%. A schematic of a hetero-junction laser diode is given in figure 3.1.
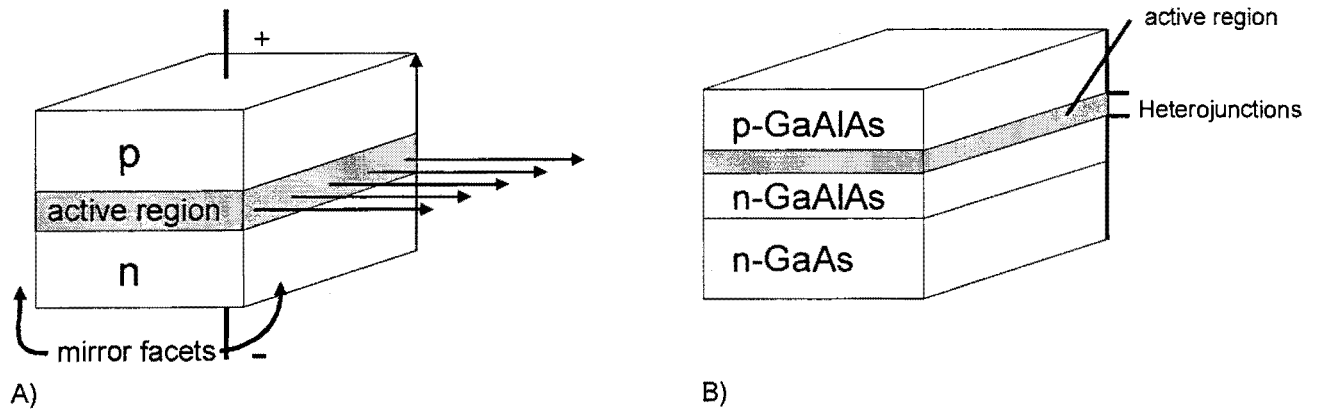
Figure 3.1 Schematic drawing of A) a hetero- and B) a double hetero-structure diode laser

The light is generated at the p-n junction. The p-layer is p-doted AlGaAs. The n-layer is n-doted GaAs. When a current is fed through the diode, light is produced at the p-n junction in a region around the junction. This active region has a typical height of 1 μm. The first diodes had to be operated at 70 K to prevent damage to the diode due to the high currents necessary to get laser working.

By adding a thin layer of another type of semi-conductor material between the p- and n-layer the characteristics of the laser diode were improved in the so-called double hetero-junction laser diode (see figure 3.1-B). The extra layer has a smaller band gap than the p-type AlGaAs and creates a potential barrier for the charge carriers. The carriers accumulate (carrier confinement) in the barrier and add to the population inversion process. Due to the higher carrier density in the active region the amplification per round trip increases, lowering the threshold current of the system.

Due to the typical sizes of the active region the laser beam is strongly divergent and if the beam is not confined to the active layer most of the created light is absorbed in the enclosing material. In the double hetero junction laser diodes, the emitted light is confined in the extra layer by total internal reflection due to the higher refractive index of the extra layer. With this extra layer the threshold current of the first laser diodes dropped from 60 kA/cm^2 to 8 kA/cm^2, which was such a major improvement that the laser diodes could be operated at room temperature in pulsed mode.

With the extra layer, the beam is confined in the transversal direction perpendicular to the active region, however in the transversal direction in the plane of the active region the beam is not confined. Therefore multiple transverse modes are present in the beam and the spatial beam quality of the laser diode is poor. To improve the quality of the laser beam, light gain- and index-guided laser diodes were developed.

In gain guided laser diodes the electrical contact is reduced to a stripe of material, with which the current is channelled through the layers and creates a transversal "confinement" of

the laser beam. Figure 3.2 shows schematic drawings of a gain- and index-guided or buried hetero-structure laser diode.

By creating a channel as the active region instead of a layer, transversal confinement is achieved in index-guided laser diodes. The size of the active region typically is 300x3x0.3 μm. This type of laser diode operates in transverse single mode and has very good optical and electrical characteristics as will be shown in the next paragraph. All of these types are often referred to as Fabry-Perot laser diodes because of their optical resonator cavity.

gain-guided stripe   index guided (buried hetero structure)

A)   B)
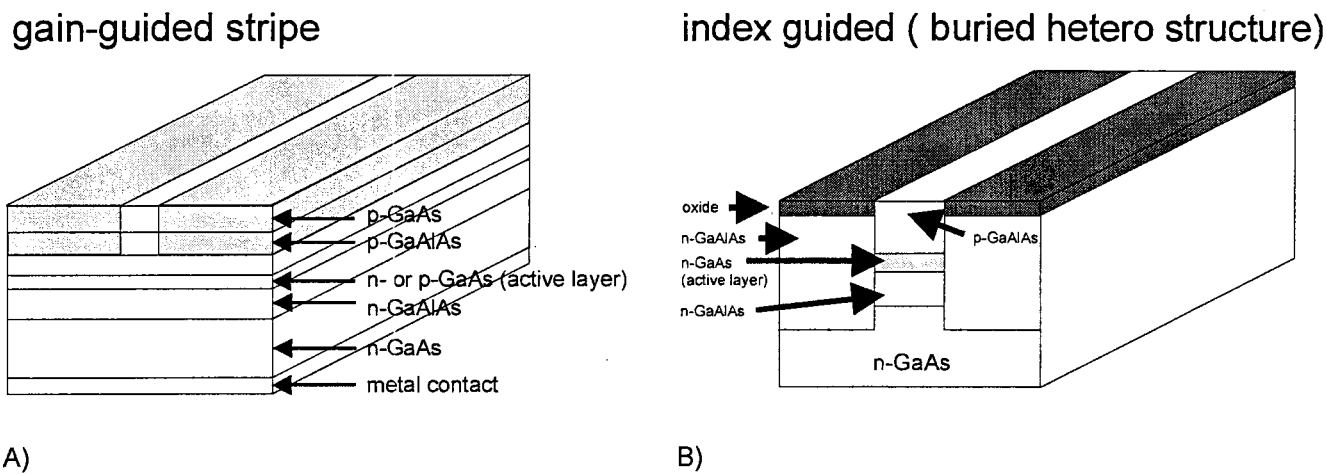
Figure 3.2 Schematic of A) a Gain-guided laser diode and B) an index guided laser diode.

Transversal confinement of laser light with: A) A striped electrical contact in gain guided laser diodes B) and a channel in Index guided or buried hetero structure laser diodes.

3.3 Optical characteristics of laser diodes

An optical resonator has multiple modes. The frequency difference between the modes is dependent on the cavity length and the refractive index of the material in the cavity and is given by equation 3.1.

$$\Delta \upsilon = \frac{c}{2nl}$$ (1)

The optical resonator of a laser diode has a typical length of 300 μm and the refractive index of GaAs is around 3,66. For a laser diode operating at 640 nm, it follows that the mode spacing is around 0,2 nm. Since the amplification per round trip or gain is above one for a broader wavelength range than 0.2 nm, multiple modes are amplified in the active region and the laser diode emits multi mode light. The modes are single spectral lines. Figure 3.3 shows the typical spectra emitted by a gain guided and index guided laser diode.
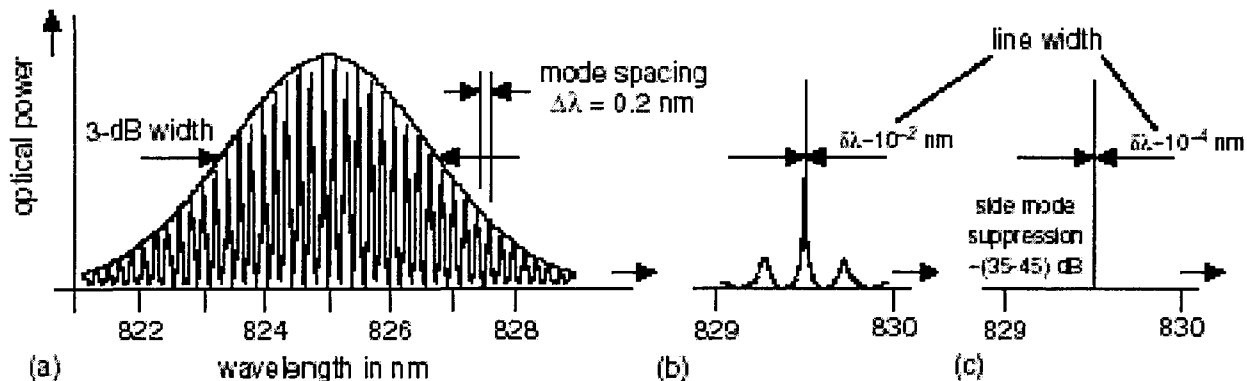
Figure 3.3 Spectra emitted by laser Fabry-Perot laser diodes: (a) a gain guided laser, (b) an index guided and (c) a DFB laser diode

From figure 3.3 it is apparent that the spectral characteristics of gain guided laser diodes and index-guided laser diodes differ. To get an idea of the effect of these differences we consider a few of the requirements for the application of laser diodes in absorption spectroscopy:

- The laser must operate in single mode to be able to perform measurements in a spectral region with many other lines present. Multiple modes make it impossible to distinguish between the absorption of the different modes and single mode operation is preferred.

- The line width of the emitted mode must be much smaller than the absorption profile width. As we will see in chapter 4 a line width that is much smaller than the line width of the absorption line width is needed to resolve the line profile.

- A mode-hop free tuning range that is much larger than the line width of the absorption profile, which is needed to resolve the wings of the profile.

- High power output for highest signal to noise ratio and suppression of the broadband background emission of the plasma in direct absorption, i.e. no modulation techniques

- The emitted laser light must match the selected absorption lines of the species.

From figure 3.3 it is clear that gain guided laser diodes have poor characteristics for the application in spectroscopy experiments. The characteristics of an index guided laser diode are much better, but to directly resolve a line profile with a full width at half maximum width (FWHM-width) of 0.01 nm is virtually impossible since the line width of the diode is of the same order and a convolution of the laser line and the absorption line profile will be measured.

To improve the line width characteristics of laser diodes, a wavelength selective device was added to the laser diode. In the Distributed Feed Back Laser diode (DFB) a wavelength selective device is added inside the optical cavity; a Bragg reflector (see figure 3.4 A and B). The Bragg reflector reflects only one mode. In a Distributed Bragg Reflector (DBR) laser diode the reflector is situated outside the cavity. Both laser types operate in single mode with a typical line width of 10^{-4} nm, which is thin enough to measure absorption profiles with a line width of 0,01 nm and therefore seem excellent candidates for our experiments.

N			N	
Active region		DBR	active region	DBR
P			P	

A)   B)
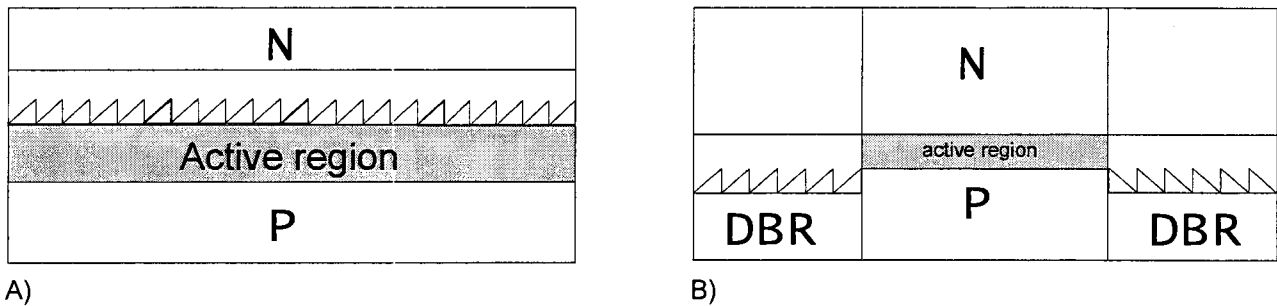
Figure 3.4 Schematic drawings of A) the distributed feedback laser diode and B) the distributed Bragg reflector laser diode

Beam properties

In the beginning of this chapter it was stated that the optical cavity of index and gain-guided laser diodes have a typical cross section of 3x0.3 μm. The length and width of the exit facet are small in comparison to the wavelength and diffraction of the beam at the facet is the result. Since the cross section is rectangular the shape of the beam becomes elliptical instead and highly divergent (see figure 3.5). To correct for the strong divergence, special fabricated optics are used.
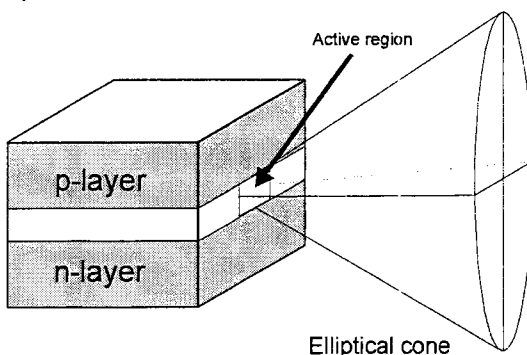
Figure 3.5 Typical beam shape of a laser diode

To improve the beam characteristics the VCSEL diode or Vertical Cavity Surface Emitting Laser Diode was developed. In the design the light is emitted perpendicular to the p-n junction as is depicted in figure 3.6. The cavity lies in the vertical direction and has a circular aperture and the beam exits at the top of the laser diode. The laser beam has a circular shape and is not as divergent as the beam from Fabry-Perot type laser diodes. The optical resonator consists of multiple layers of material that act as Bragg-reflector. The part below the active region contains around 40 different layers and the top part 25. The resonator design also means that the output of the diode is single mode and the line width is typically smaller than 100 MHz at 780 nm. The output is single mode over several nm with temperature tuning [12].

The typical tuning rate is 0.3 nm/mA for current tuning and 0.06 nm/ °C for temperature tuning.
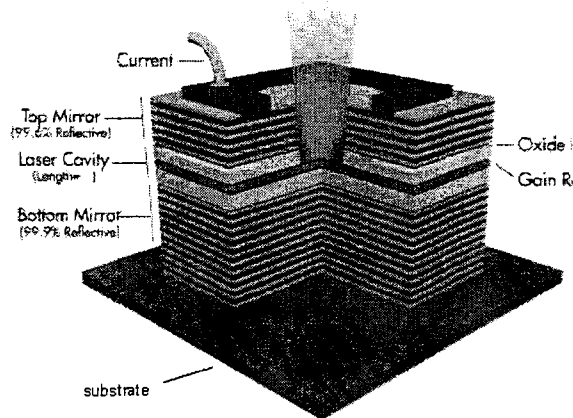
Figure 3.6 Schematic overview of a Vertical Cavity Surface Emitting Laser diode

3.4 Temperature dependence of output wavelength and power

Laser diodes are temperature dependent devices. The optical power output of a laser above the threshold current is linearly dependent on the current like in figure 3.7-B. The figure shows the optical power-current behaviour for 3 different temperatures.

There are two interesting features that are important. The first is that the threshold current at which the laser diode starts lasering increases with temperature and since the maximum current running through the laser diode is more or less fixed, the maximum achievable optical power decreases with higher temperatures. This shift in threshold current originates from the temperature dependence of the carrier concentration in the active layer. The second feature is that with increasing temperature the change in optical power output with the current decreases, i.e. the slope of the lines decreases.

The temperature not only influences the power characteristics of the diodes, but also the spectral characteristics of the emitted light. With increasing temperatures the semi-conductor material will extend and the optical resonator will get larger. At the same time the refractive index of the material increases and the emitted modes will shift to longer wavelengths.

The amplification- or gain-curve also shifts to longer wavelengths as the band gap decreases with increasing temperature. The shift in wavelength in the emitted modes is lower than the change in the gain curve and at a certain temperature the emitted wavelength hops from the emitted laser mode to another. In single mode operation this effect is clearly visible. Figure 3.7-A shows a typical mode hop structure of an index guided laser diode.

27
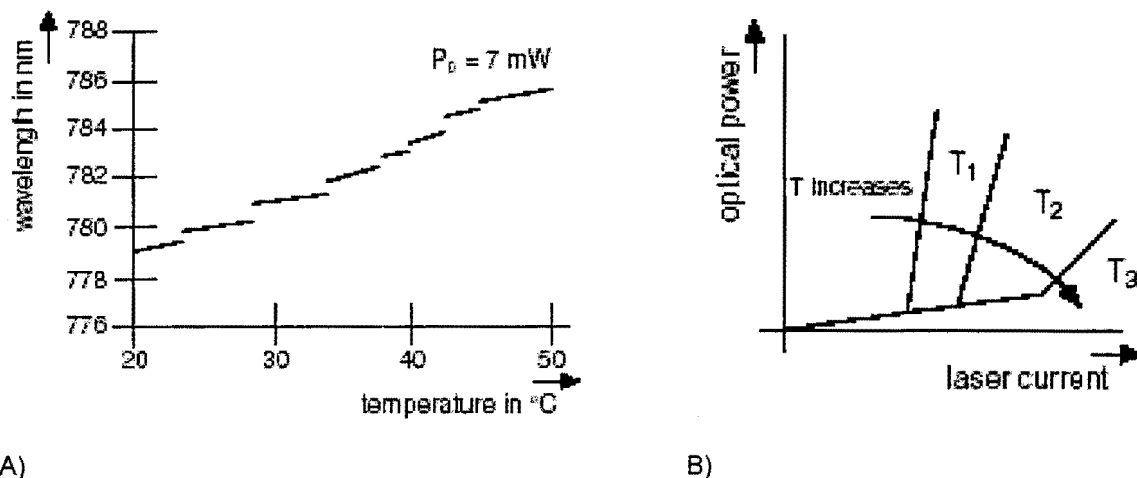
Figure 3.7 A) Typical temperature dependence of the output wavelength of a Fabry-Perot type laser diode B) Typical output power current characteristic of an index guided laser diode for different temperatures.

The typical effect of the temperature on the output wavelength between two mode-hops is between 0,12-0,25 nm/K for index-guided laser diodes and 0,02-0,1 nm/K for DFB and DBR laser diodes. This means that the wavelength of a laser diode can be tuned by changing the temperature.

The tuning of gain- and index-guided laser diodes is however limited. Due to the mode structure not all wavelengths are attainable and if the laser diode has a mode hop in the spectral region of interest there is only one alternative and that is trying another laser diode. Therefore some manufacturers have constructions in which they send a package of diodes, from which a suitable diode can be selected.

DFB and DBR lasers do not show mode hopping, due to the fact that the Bragg reflector reflects a typical wavelength only the mode with that particular wavelength exists. Even if the length of the cavity changes by changing the temperature and or the power generated in the junction the output wavelength is determined by the reflected wavelength of the reflector.

Another way of tuning the laser diodes is by changing the laser current. The effect of higher currents besides the higher optical power output is heating of the active region and as a result the output wavelength shifts to longer wavelengths. A typical value for current wavelength tuning is 0.05 nm/mA. If high stability of the wavelength is required and/or at different currents, the temperature of the laser diode must be controlled, in practice this is often achieved with a Peltier element and a temperature control unit. The various characteristics of the described laser diodes are summarised in table 3.1

Table 3.1 Overview of the properties of the discussed laser diodes

Properties	Fabry-Perot lasers	DFB and DBR laser diodes
Emission properties	Strong temperature dependence with mode jumpping and a tuning	Only single mode operation, tuning of 0,02-0,1 nm/K

	rate of 0,12-0,25 nm/K	
Line width	Wide, typically 10^{-2} nm	Narrow, typically 10^{-4} nm
Spectrum	Multi mode spectrum with with a typical mode separation of 0,2 nm	Only single mode operation
Mode hop free tuning range	Typically around 0.01 nm @ 640m	No mode hopping

3.5 Wavelength Tuning with an external cavity

For the application in absorption spectroscopy the laser diodes with the Bragg reflectors seem excellent candidates, but there is a minor glitch. The laser diodes do not operate at the wavelength of the selected absorption lines.

Laser diodes and especially the DFB and DBR diodes are not available in the whole spectrum. The main application of laser diodes is in the telecommunication market and applications like cd-players/burners, bar-code readers and laser printers. Therefore a lot of research and development has focused on the development of specific wavelengths. For the telecom market 1300 and 1500 nm were developed because the optical properties of glass fibres are optimal for those wavelengths. Therefore laser diodes are available in a limited region or at distinct wavelengths.

In HID lamps most of the additives have most of their emission lines in the visible region of the spectrum, making them excellent candidates for lighting applications. As we will see in chapter 4 the region of interest is between 641 and 644 nm, therefore the DBR or DFB laser diodes to study the salt additives with absorption spectroscopy are excluded as an option. Index and gain-guided laser diodes are available from 630 nm and up. Their poor tuning and optical characteristics make them not very suitable for use in a space mission, since the mode structure of the diodes is different for each diode and the mode structure might change over time. Therefore a system that is capable of tuning the wavelength of laser diodes in the visible region over a large wavelength range without mode hopping or wavelength regions that cannot be used is needed.

We have seen that the line width of laser diodes and mode behaviour can be improved by using a wavelength selective device like a Bragg reflector. In the last two decades laser systems have been developed that use an external grating for the wavelength selection, similar to the Bragg reflector. The difference between the Bragg reflector devices and the grating based systems is that the grating is situated outside the laser diode like in figure 3.8.

To be able to use the grating the optical resonator of the laser diode is extended by coating one of the end facets of the laser diode with an anti-reflection coating. The coating makes the facet transparent for light coming from the outside and light reflected by the grating is coupled back into the cavity of the laser diode. In this way the reflected light determines which wavelength is amplified and therefore the output of the laser diode.

Rotating the grating gives not only an extra way of wavelength tuning, it also makes it possible to obtain all wavelengths by moving the mode structure by changing the operating temperature. Even the wavelengths that were unattainable due to the mode structure are available in these systems. This type of diode laser system is build by various companies over the world (Sacher Laser Technik, Toptica, Eosi, Newport, ILX).

There are two different types of configuration of the grating in the system; Littman and Littrow based. Figure 3.8 shows a schematic of both systems.

A) Littmann configured wavelength selection

B) Littrow configured wavelength selection
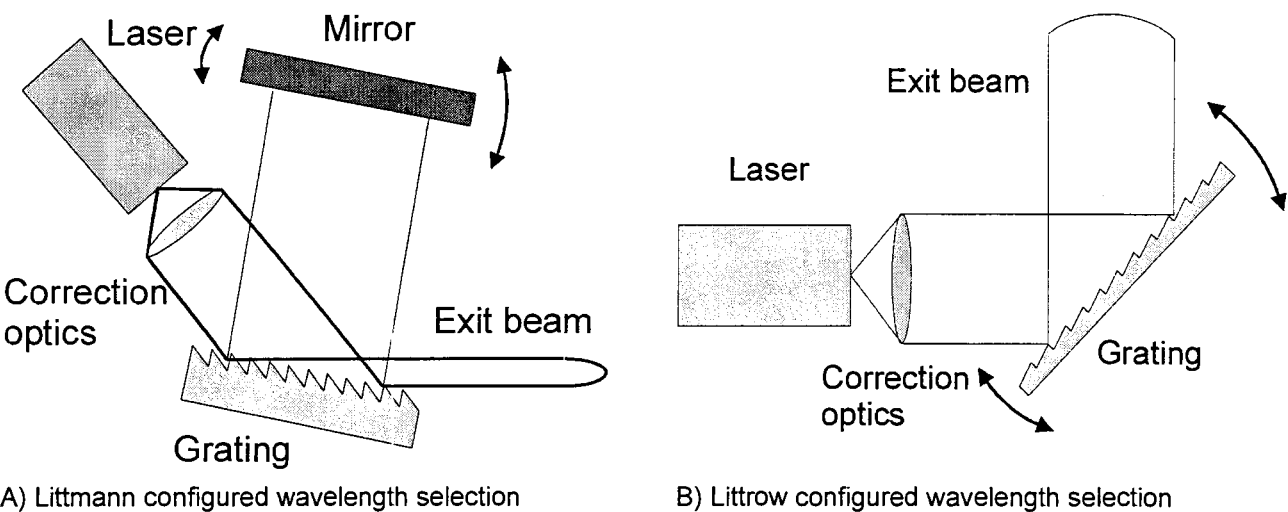
Figure 3.8 Schematics of Littmann and Littrow configured TECDL systems

The main difference between the systems is that in the Littrow configuration the tuning is achieved by rotating the mirror and in the Littmann configuration by rotating the grating. When the wavelength is widely tuned, the exit beam changes direction due to the rotation of the grating in the Littmann configuration.

In the Littrow configuration this is prevented by using a rotating mirror that reflects the first order of the diffracted light. In this way the grating angle is fixed and the exit beam does not change in angle or position with tuning. Table 3.2 summarizes the characteristics of the two external cavity diode laser systems.

Table 3.2 Overview of the properties of Littrow and Litmann ECDL systems

Properties	Littmann configuration	Littrow configuration
Emission properties	Single mode over a limited range	Single mode over a limited range
Line width	< 0.5 MHz	< 2 MHz, typically 1 MHz
Spectrum	Single mode at any wavelength within the coarse tuning range, but still with mode hops	Single mode at any wavelength in the coarse tuning range, but still with mode hops
Coarse Tuning range	> 10 nm depending on the type of laser diode	> 10 nm depending on the type of laser diode
Mode hop free tuning range	> 0.04 nm depending on the wavelength region	> 5 GHz at any available wavelength

Beam characteristic	Exit beam is identical for all wavelengths	Changes in exit angle and position with coarse tuning

Based on the requirements needed in absorption spectroscopy, the selected salt-additives, the spectral lines that will be selected and the requirements in operating a system in the ISS a suitable diode laser system has to be selected. From the previous sections and the spectroscopic requirements listed in paragraph 3.3, an external cavity system remains as the only suitable option. In the next chapter all the requirements to select a laser system will be described and the choice of laser system that resulted from it will be described in chapter 5. The following table summarizes the typical characteristics of the described laser diodes and diode laser systems. It must be noted that values are typical values and that the characteristics change with output wavelength.

Table 3.3 Typical characteristics of laser diodes [13], [14], [15], [16]

Type	SM/MM	$\Delta\lambda_{Free}$	λ_c	MJ	LW	BS	OP	SS	TR	TTR
Gain Guided	MM	0.005	410-420,630-700,730-1090, 1250-1650	Y	3nm	E	>3	-	0.05	0.06
Index Guided	SM/MM	0.005	410-420,630nm-2μm	Y	0.01 nm	E	>3	35-45	0.05	0.06
DBR	SM	-	1.20-1.68μm	N	10^{-4} nm	E	>0.5	>20	0.1	0.02
DFB	SM	-	1.20-1.68μm	N	10^{-4} nm	E	>0.5	20-40	0.1	0.1-C
VCSEL	SM/MM	-	780,850	N	< 50 MHz	C	0,3/5	>20	0.2	0.05
ECDL Littrow	SM	>0.04	630-700,730-1090,1250-1650	Y	< 10 MHz	E	>3	35-45	0.0004	-
ECDL Litmann	SM	>0.04	630-700,730-1090,1250-1650	Y	< 10 MHz	E	>3	35-45	0.0004	-

With:

SM/MM Single Mode or Multi Mode operation,
$\Delta\lambda_{Free}$ typical mode hop free tuning range,
λ_c the available wavelength regions,
MJ Mode Hoping,
LW the typical line width,
BS the beamshape (E = elliptical, C =circular),
OP the Output Power, SS Side Mode Suppression [dB]
TR Current tuning rate in [nm/mA],
TTR Temperature Tuning Rate [nm/k]

4 Design Requirements

4.1 Space compatibility

Going into space demands very high performance from material and construction. During launch of the spacecraft strong vibrations, both acoustic and mechanical, and accelerations result in high levels of stress and strain in the payload. An even more important issue in space flight is safety. It is of the utmost importance that any kind of object during launch or operation in the space station cannot cause any problems that will affect and or endanger the crew on board in any way, therefore hazardous materials like mercury and krypton[85] in the HID-lamps need triple-containment and the setup must be controllable from outside the containment layers.

A third and also very important parameter of space flight is the weight. To bring a kg of material to the ISS takes an immense amount of energy and the price associated with the transport of a kg from earth to the ISS lies around EUR 30000,-. Therefore a lot of effort is put into minimizing the weight of objects that need to be launched and the use of very expensive, but light materials, in the design can save an enormous amount of money. The project will participate in an ESA mission, where for the total space mission 85 kg has been reserved on the Progress freight flight. The weight estimation of the total setup was initially estimated at 15 kg, but has gradually increased to 29,5 kg due to the various extra-unforeseen demands and the required flexibility in the placement of the setup in the Russian- or American-section of the ISS.

Not only the weight, but also the volume is a limiting factor. For instance the space available inside the MSG (Micro gravity Science Glove box) of ESA and the diameter of the doors limit the maximum volume that can be used, which is around 20 litres for the total setup.

Another limitation in operating a setup in the ISS is the available electric power. The amount of electrical power that can be drawn from the outlets is limited to 220W in the Russian section and to 800W in the MSG. Since the HID-lamps will be operated at 150W by a power supply unit that consumes 10W, 40W is available for operating the laser system and data-acquisition system (The emission spectrometer will be switched off during operation of the laser setup).

When consuming 220W of power in a closed system the consumed power will be converted to heat and must be removed by active cooling, since in zero-gravity convection based cooling will not work. The cooling capacity of the system is bound by specifications of the space agencies and unfortunately differ for the Russian and American section. Due to the limitations of the maximum amount of cooling power in both sections, the operating temperature of the experiment will be up to 40 degrees Celsius and will most likely fluctuate due to the change of the environmental temperature. The maximum allowed temperature of the cover of the setup is 45 degrees Celsius for human safety reasons.

It is clear that there are a lot of requirements to build a space compatible setup. For the laser absorption part the requirements important for the initial design can be summarized to:

- Power usage limited to 40 Watt for the laser absorption system and data acquisition system.
- Laser system capable of operating around 40 degrees Celsius.
- Design must be compact due to volume restrictions (For the whole setup 20 l).
- Mechanically stable and strong enough to survive launch and keep optically aligned.
- System must survive temperature changes during launch and must be insensitive to temperature changes in the environment.
- The design must be as light as possible due to the weight limit
- System must be remotely operable from outside the containment layers.

4.2 Line selection and spectroscopic requirements

The combination of emission spectroscopy with absorption spectroscopy to study Cerium salt-additives in HID-lamps will result in a more complete picture of the particle distribution; both ground state and excited states of neutrals and ions can be monitored and compared. To combine the results of both methods it is preferable to use absorption and emission lines that are in the vicinity of each other.

The method that will be used to determine relative particle densities with emission spectroscopy is based on the intensity ratio of two emission lines with an upper energy level difference of at least 1 eV, that are relatively close in the spectrum and are near a strong emission line. The reason for this is that the strong emission line is an extra indication for the lines to be optically thin, which is required to use the emission lines for an estimate of the plasma temperature [17] and the difference in energy level gives the opportunity to retrieve the temperature from Boltzmann plots with high enough accuracy. Therefore the line selection for the absorption- and emission-setup were combined.

For the absorption measurements the selected lines need to be resonant or very close to resonance and need to be optically thin enough to ensure absorptions of less than 10 percent to approximate the Lambert-Beer-Law without large deviations, which translates into an optical thickness of around 1. Furthermore the transition probabilities, degeneracy's and energy levels must be known [31].

Commercial laser diodes are available from 630 nm up too higher wavelengths; anything below 630 nm is simply not possible (although there are recent developments in the blue region). The Cerium salt additive emits in the wavelength region roughly up to 750 nm. Therefore the selected lines need to be found in the spectral region of 630-750 nm. From this we obtain several requirements for the selection of suitable absorption lines:

- Lines must be resonant or near resonance

- Suitable emission and absorption lines exist in the same wavelength region
- Optical Thickness $\cong$ 1
- Lines lie within the spectroscopic region of 630-750 nm
- Lines are optically isolated, i.e. no interference from other lines
- Emission lines exist in the vicinity with an upper energy level difference $\geq$ 1 eV

To estimate the optical thickness of the Cerium lines, the optical thickness was calculated with [7], [17]:

$$\tau_0 = 2k_0 R_{eff} = 11.06 \cdot 10^{-5} \frac{\langle n_{ce} \rangle R_{eff} f_{Ce} g_l \exp(-E_l / kT_{plasma})}{Q(T_{plasma}) \pi \delta \upsilon} \tag{4.1}$$

Where R_{eff} represents the radius of the lamp-burner, $\langle n_{Ce} \rangle$ the averaged number density of Cerium atoms, f_{Ce} the oscillator strength associated with the transition, g_l the degeneracy of the lower energy state, E_l the energy of corresponding lower level, T_{plasma} the average plasma temperature, $Q(T_{plasma})$ the partition sum for Cerium at the average plasma temperature T_{plasma} and $\delta \upsilon$ the FWHM-width of the particular line. For all the known Cerium lines in the region from 620-750 nm we calculated the optical thickness with the following assumptions:

- R_{eff} = 2 mm
- $\langle n_{Ce} \rangle \approx 10^{21}$ m^{-3}
- f_{Ce}, g_l and E_l from the Kurucz database [7]
- T_{plasma} = 5000 K
- $Q(T)$ = 190 (Calculated from all the energy levels in the Kurucz database for T=5000 k)
- $\delta \upsilon$ = 7.25 GHz (0.01 nm)

From these calculations and the previously stated requirements one suitable absorption line for cerium was found in the visible region of the spectrum. Initially Cerium was the only element that would be measured and scandium was selected as an emergency-backup option in case the measurement of cerium would not be possible. During a later stage of the project dysprosium was added to the list as an interesting additive to measure. For both scandium and dysprosium lines were found in the spectral region of the at that time already selected and bought laser system. In the table below the selected lines have been listed and measured spectra of the additives around the selected lines are given in figure 4.1. More details of the species, the selected lines and the calculated values of the partition sums for the species, are given in Appendix C

	Cerium	Dysprosium	Scandium
τ_0	0.49	3.76	3.10
λ	643.3488	642.1913	641.3324
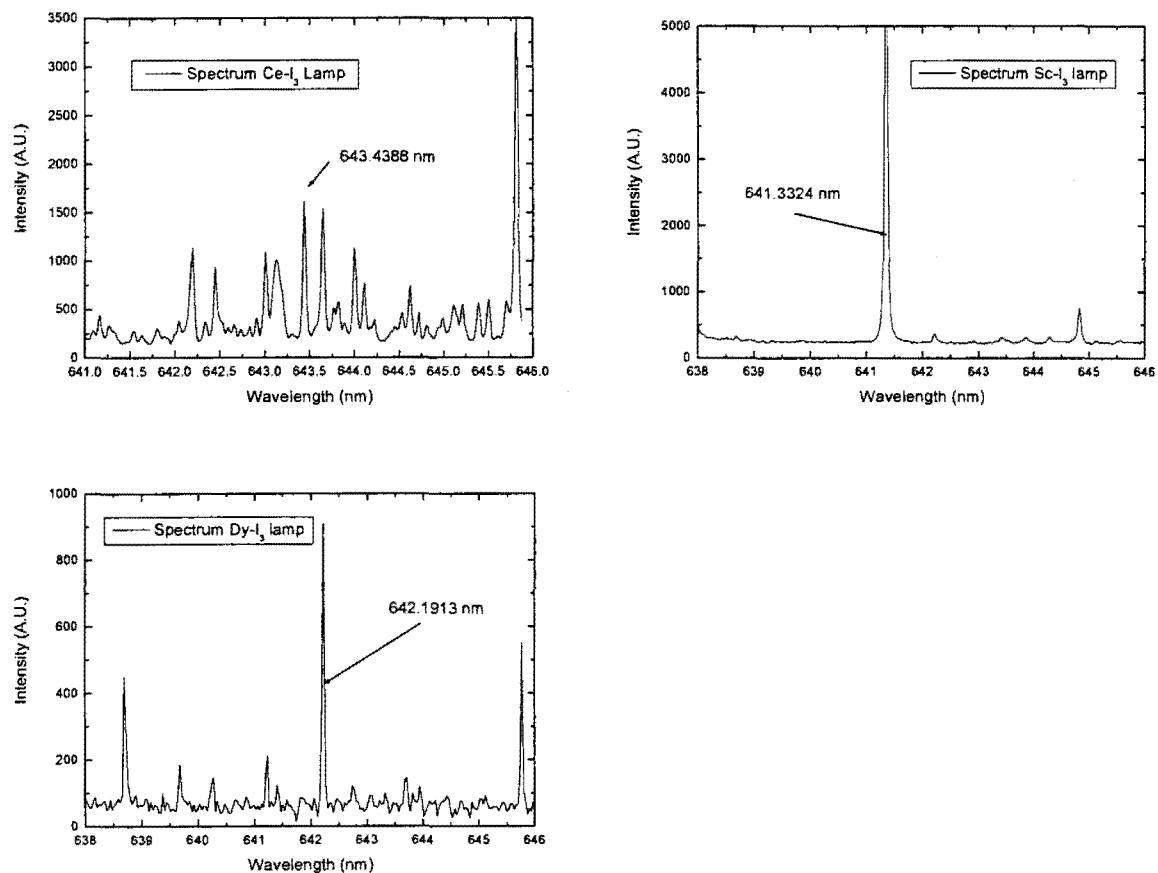
Figure 4.1 Spectral regions around the selected additive lines taken from measurements taken at Philips Central Development Lamps.

5 Experimental setup

Based on the requirements listed in the previous chapters a commercially available laser system was selected and an optical system was designed to overcome problems associated with the used geometry of the quartz burners. In this chapter each of the major components and the system that was designed and build for 34th parabolic flight campaign of ESA will be described.

5.1 Overview of the setup

The setup designed for the parabolic flights contains a lamp carrousel in which 20 lamps can be mounted. By rotating the carrousel a lamp can be moved into the measuring position, after which it can be ignited and the experiments can be performed.

In figure 5.1 an overview of the setup is given. The setup contains 3 separate diagnostic systems to study the quartz- and PCA-lamps; the laser diode absorption setup, the emission spectrometer and a Philips web cam to study the helical instabilities in the PCA lamps.
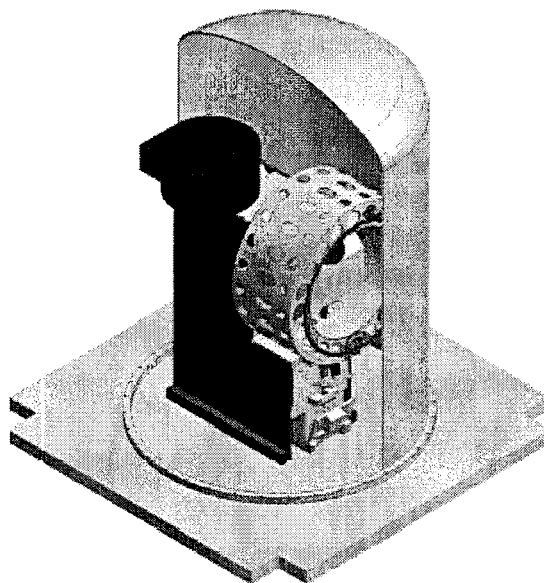
Figure 5.1 Schematic of the total setup used in the parabolic flight campaign, with on the right side the lamp carrousel and on the top left the CCD camera of the spectrometer. The tunable diode laser system is situated at the bottom of the frame, below the lamp carrousel. The lever construction with the mirror mount and the first cylindrical lens of the optical system can be seen.

The optical systems, the laser absorption system and the lens mounts are shown in more detail in figures 5.2 and 5.3. The side views of the optical systems show the beam path of the

laser beam and the imaging trajectory of the spectrometer. All of the components of the laser absorption setup will be described in more detail in the following paragraphs.
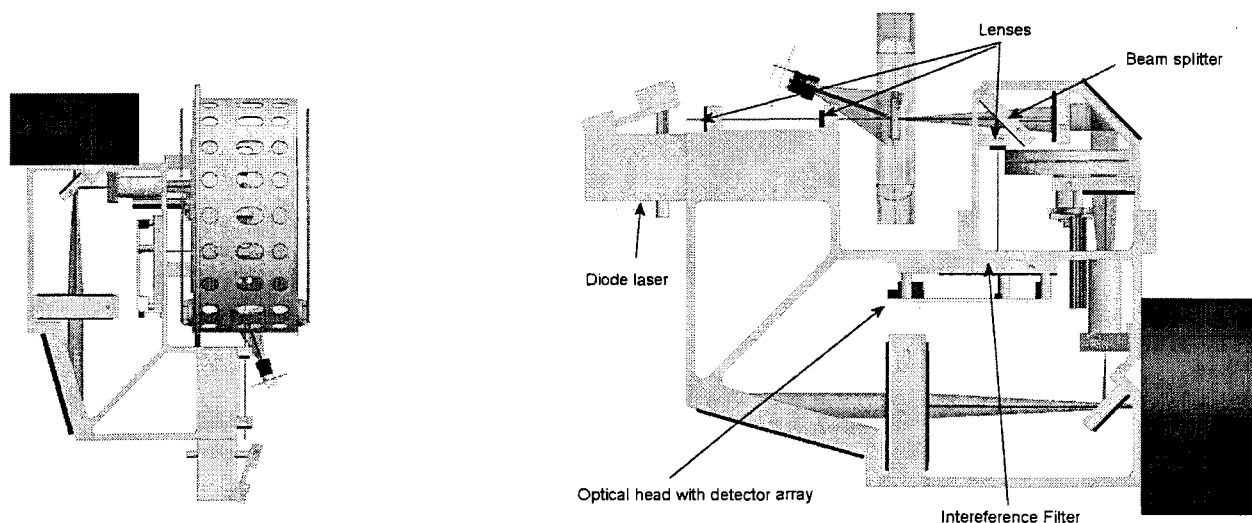
Figure 5.2 Side views of the optical design of the laser absorption setup and spectrometer with and without the lamp carrousel
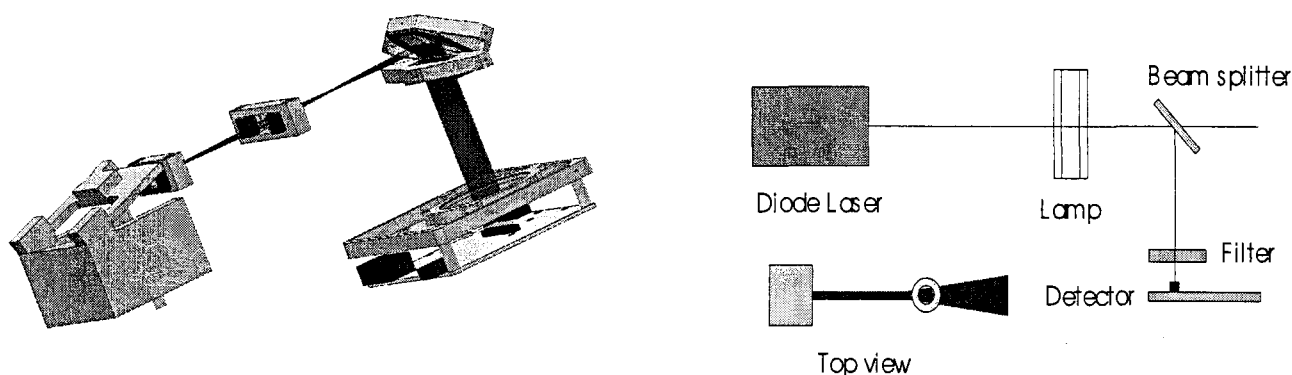
Figure 5.3 Left: Image of the optics of the laser absorption setup with the cylinder lens system, beam splitter, filter mount and detector head. Right: Schematic of the optical configuration and top view of the laser beam path through the lamps

5.2 External Cavity Tunable diode laser system

In section 3.3 and chapter 4 the spectroscopic and initial space requirements of the laser system were listed. Combining these, the laser absorption system has to meet all of the following requirements:

- Single mode operation of the laser diode over a large enough range to probe the complete line profiles.

- A laser line width that is much smaller than the absorption profile width. $\delta v \ll 3.6$ GHz
- A mode-hop free tuning range that is much larger than the line width (a FWHM of 0.005 nm) of the absorption profile to resolve the wings of the line profiles.
- High power output for highest signal to noise ratio and suppression of background emission of the discharge.
- Operation at the selected absorption line for Cerium: 643.4388 nm.
- Power usage is limited to a total of 40 Watt for the laser absorption system and data acquisition system.
- Capability of operating around 40 degrees Celsius.
- Design must be compact due to volume restrictions (For the whole setup 20L).
- Mechanically stable and strong enough to survive launch and keep aligned.
- System capable of surviving temperature changes during launch and insensitive to temperature changes in the environment during operation.
- Design must be as light as possible due to weight limitations on the Progress flight.
- System must be operated remotely, i.e. from outside the containment layers.
- Obtain lateral information up to at least 80% of the burner diameter

After an extensive search for different options an external cavity diode laser (ECDL) seemed the only available option. Mainly the output wavelength and the selected absorption lines and the mode hop free tuning ranges did not match for the other types of laser diodes and diode laser systems.

Considering the short period of time available due to the new and much earlier launch date it was preferred to use as many standard components as possible with short delivery times. From various manufacturers of ECDL systems the best option for our purpose was a system built by Sacher Lasertechnik The system as it comes off the shelve meets most of the requirements. Figure 5.4 shows a picture of the inside of the unmodified TEC 500 laser head, the technical specifications of the system are listed in table 5.1.
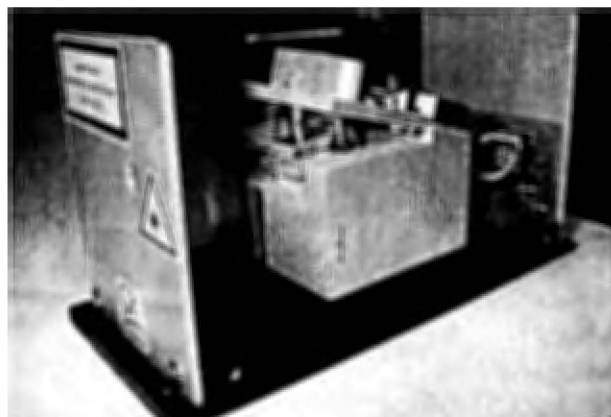
Figure 5.4 Inside of the unmodified TEC 500 laser head. The mirror mount and grating are visible. To give the reader an idea of the size of the head; the metal block in the middle can be compared with the size of a fist.

Table 5.1 Technical Data of the TEC 500-0645-03 Lion laser system [13]

Output Wavelength	640-650 nm
Coarse Tuning Range	10 nm
Fine tuning range	0.5 nm
Fine tuning range mode hop free	> 30 GHz
Output Power	> 5mW
Line Width (20 s)	< 5 MHz
Frequency Modulation	0.5 kHz @ 10 GHz frequency change
Long term drift (24 hr)	300 MHz
Side mode suppression	40 dB
Beam profile	Elliptic ratio = 1:4
Maximum cooling power Peltier element	16 W
Laser current	<100 mA
Dimensions laser head lxwxh	165x80x93 mm
Dimensions cooling mount lxwxh	70x70x80 mm

A Littmann configured ECDL system was bought because of its excellent beam characteristics over large wavelength tuning ranges. The system is also available in a Littrow configuration, in which the tuning is achieved by rotating a grating and the laser beam rotates with the grating. In the Littmann configured system this is prevented by rotating a mirror instead of the grating and use the zero-th order of the grating as the exiting laser beam. Both configurations were described in more detail in chapter 3, schematics of both configurations were pictured in figures 3.8-A and –B.

The wavelength tuning of the ECDL system is achieved by moving a mirror with a Piezo-element. The set voltage over the Piezo element determines the output wavelength within the specified 0.5 nm tuning range. The amplifier in the MLD-1000 controller unit controls the Piezo element by putting a DC voltage between –10 and 100 volts over the Piezo element.

The applied voltage to the Piezo element is the result of the manual setting of the control knob on the controller together with the voltage applied to the analogue input on the controller. The analogue input signal is amplified 10-fold and the full scanning range can be obtained by applying a DC voltage between –1 and 10 volts on the analogue input.

The wavelength of the ECDL system can also be modulated over a large range with a modulation frequency up to 1 kHz around the set centre wavelength by applying a periodic signal to the analogue input of the Piezo amplifier. For this purpose, the developed TU/e DACS control system, which will be described in section 5.4, is capable of generating a saw-tooth signal with an amplitude adjustable between 0-10 V. The Piezo modulated tuning of the wavelength will be used to scan the laser wavelength back and forth over the absorption line profiles.

5.3 Optical design

In the right schematic of figure 5.3, the path of the laser beam has been drawn through the lamps and the top view drawing of the beam path shows that the beam exits the lamps under different angles for different lateral positions. This is caused by the lens working of the burner and BuBa. To obtain lateral resolved measurements, the laser beam must be moved to different lateral positions by moving either the lamp or the laser head. Therefore the exit angle of the laser beam would change with lateral position and the detector position would need adjustment accordingly, which would put very high demands on the mechanical positioning of the lamp carrousel or diode laser and detector. And would require complex mechanics and extra moving parts, which both are unwanted for any application and especially in space flight.

To overcome these problems the elliptical shape of the laser beam profile was used to create a laser sheet and illuminate over the whole burner diameter and instead of using one moving detector a detector head with an array of 32 photodiodes was designed and build. The laser beam is expanded along the long side of the ellipse, as depicted in the schematics of figure 5.5.

A) B)
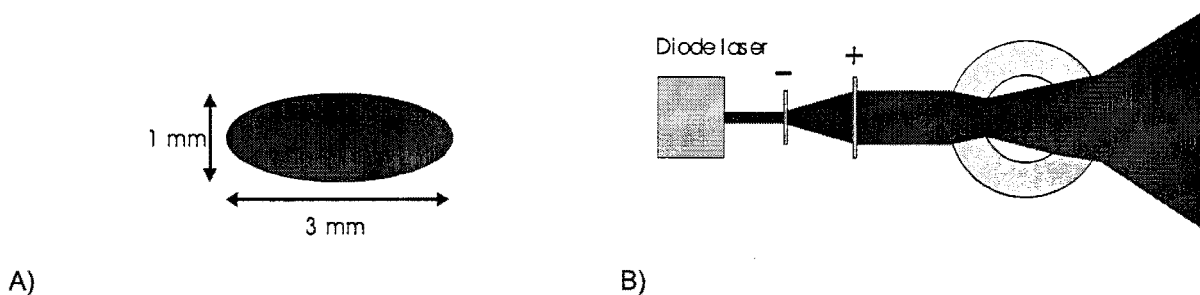
Figure 5.5 Schematic drawing of the elliptical shape of the laser beam and its propagation through the quartz lamps

To reduce the background emission of the lamp an interference filter was placed between the lamp and detector. The strong angle dependence of such filters requires that the laser light passes collimated through the filter and therefore collimating optics were needed. By ray tracing the selected lamp design with the ZEMAX [22] program, different options and configurations were tested. The various components in the configurations were chosen from a database with standard products of most of the vendors of optical components, to ensure availability and short order times.

All of the configurations were optimised to enclose the highest amount of light diffracted by the lamps, to obtain the maximum possible lateral scan over the burner diameter. The optimisation was done by defining a beam with hundreds of parallel rays of light and having the software trace each of the rays through the system, by adjusting the positions of the optical components until the optimum configuration was found, i.e. this can be compared with creating a laser sheet of the dimensions of the inner diameter of the burner and following its beam path. To make the comparison complete, a diaphragm with the elliptical dimensions of

the laser beam (as depicted in figure 5.5) was placed in the parallel beam to obtain the spot of the laser beam on the detector array.

Since the lamps are cylindrical symmetric all the interesting optical effects occur in one plane and therefore the plotted ray trace results in figure 5.6 are top views of the optical configurations and the lamps. In the pictures, the large circle is a standard BuBa and the inner small circle a standard quartz burner.

The first configuration was built up with standard plano-convex lenses. Picture 5.6-A shows the result of the ray tracing for optimised lens positions. From the figure it is clear that the exit beam is not collimated at any point, which is necessary for the use of the interference filter. Furthermore a full lateral scan over the burner diameter is not possible, which can be seen from the rays passing around the first lens. Another problem is that the first lens is positioned less than 10 mm away from the BuBa, which makes rotation of the carrousel very difficult or even impossible and extra shielding of the lens and its mount for damage by excessive heat dissipation needed.

In the second configuration a parabolic mirror was tested. The parabolic mirror reflects all of the light from the upper side of the burner but fails for the bottom part. For the upper half of the burner a full lateral scan can be made and by assuming cylindrical symmetry the bottom part could be reconstructed. The beam reflected by the mirror is a collimated beam with a width of around 8 cm, which is much wider than the available interference filters. This could have been corrected by using the opposite system of a beam expander. Although the parabolic mirror shows as a possible option, the used mirror or a similar alternative were not available within the required time and could therefore not be used.

A)

B)
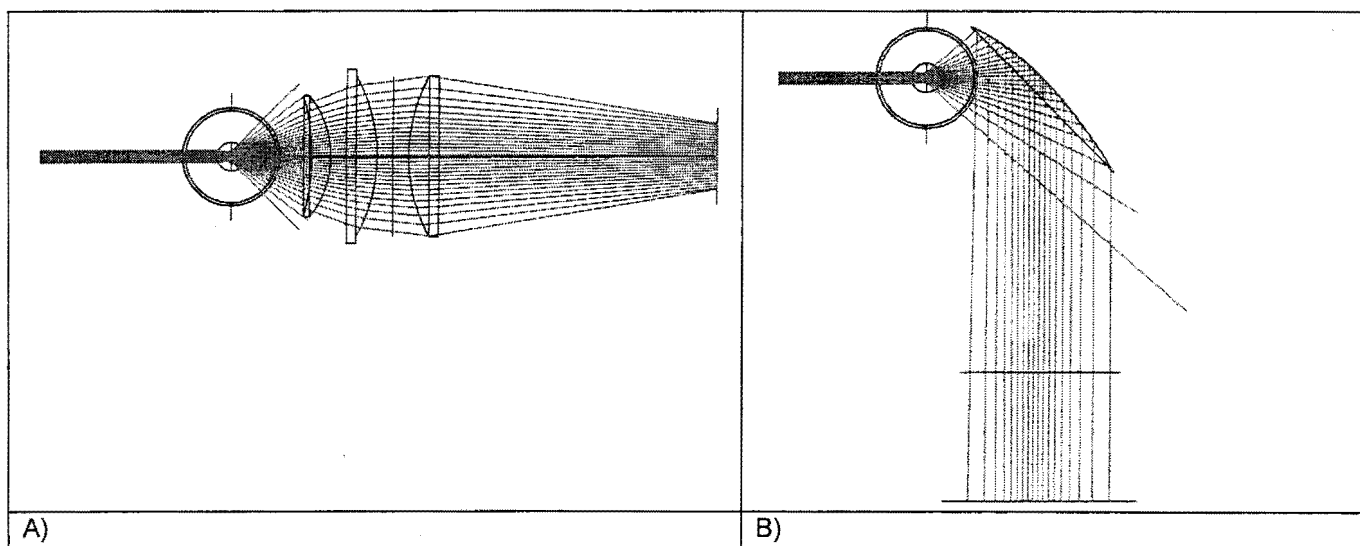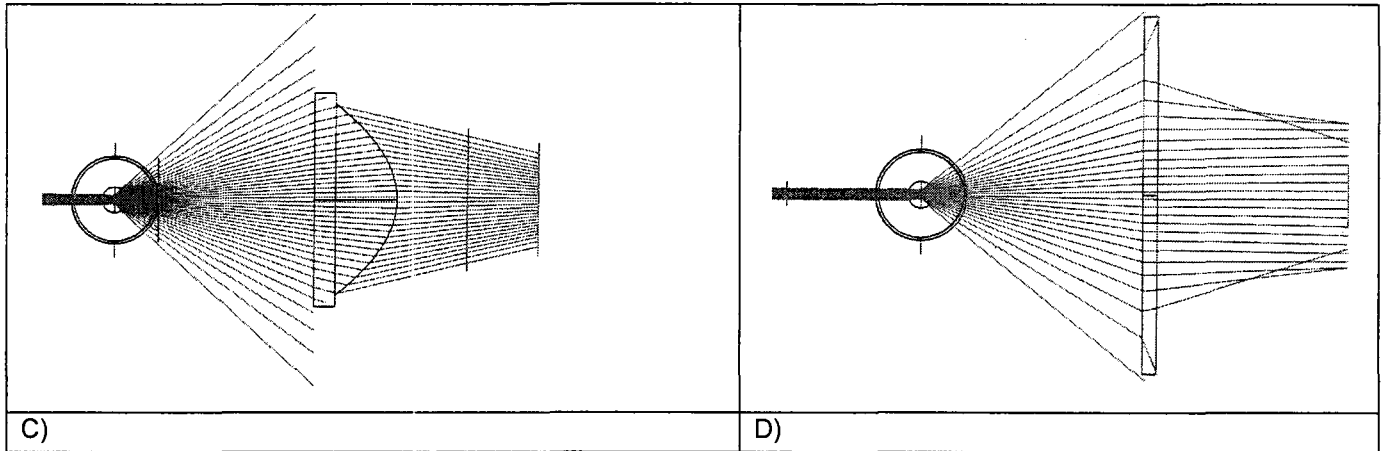
Figure 5.6 Ray trace results for various optical configurations A) a plano convex lens system with 3 lenses, B) a parabolic mirror, C) an off-axis lens and D) a Fresnel lens.

The third configuration consisted of an off-axis lens, for which the curvature of the lens changes over the off-axis position. These lenses are known to have high opening angles for short focal lengths and to have less aberration than standard plano-convex lenses. Figure 5.6-C shows that even for the best combination of focal length and diameter a lot of the light passes the lens, furthermore the beam generated by the lens would require extra correction optics to create a collimated beam for the interference filter.

The last type of component that was tested was a Fresnel lens. As figure 5.6-D shows, most of the light is imaged and only on the far edges of the lens, light is passing the lens and up to 65% of the burner diameter can be measured. Although a relatively large portion of the burner can be scanned, the resulting beam is not collimated and this type of lens was not available in the required diameter and focal length

There are a few important conclusions that can be drawn from the ray tracing. The first is that it is impossible to measure over the full burner diameter and image the divergent beam with a standard commercial available components and that the best option is the multiple lens configuration (depicted in figure 5.6-A) where up to 70% of the burner diameter will be measurable. The exit angle of the beam is too large for the opening angle of the lenses or mirrors and for the options that seem feasible, the lenses have to be positioned very close to the burner and BuBa and making rotation of the lamp carrousel impossible.

The second is that the beam exiting from three of the configurations is not collimated and extra lenses are necessary to correct the beam path to pass collimated through the interference filter.

The third problem with these designs is the non-parallel beam path through the burner, which is inconvenient for Abel-inversion. Figure 5.5-B shows the typical beam path for the ray-traced configurations and figure 5.9-A shows the preferred beam path in the burner. For Abel-inversion it is convenient if the beam path is parallel and linearly correlated to the lateral

position, if this is not the case the beam path must be known and calibrations and correction of the data afterwards will be unavoidable.

Instead of trying to obtain as much light as possible the design was altered to benefit from the lens working of the burner and BuBa and incorporate the burner as a lens system in the optical design. Figure 5.7 shows the two burner designs that were used in detail. The left burner design is the design on which the specifications, optical design and requirements of the setup were based and the first tests were performed. The right figure shows the burner design used in the parabolic flight campaign.

For the measurements in the parabolic flights it was decided to use different lamps with a bigger diameter to maximise the effect of the convective flows as predicted and measured by Fischer [18]. Therefore the first optical configuration was adapted to the burner design with an inner diameter of 8 mm, with the use of as much lenses as possible from the design for the 4 mm burner due to the short timeframe before the parabolic flights at the time.
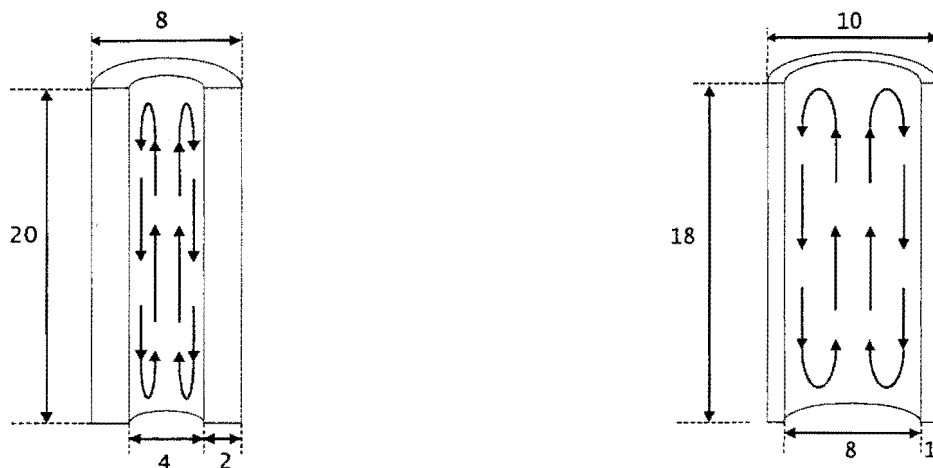
A) Burner design used to test and specify the requirements of the setup

B) Burner design used in the parabolic flights

Figure 5.7 Used burner configurations.

Both burners are standard quartz designs with a relatively thick burner wall, which causes the very strong negative cylinder lens working. Both burner designs were built into 22 mm inner diameter BuBa's with a wall thickness of 1 mm.

To incorporate the burner design in the optics and use the lens working of the burner, the laser beam was expanded in one direction and focused with a positive lens in a way that the burner expanded the focused beam in such way that it can easily be collimated with a standard lens and passed through an interference filter and imaged on the detector array. Figure 5.8-A shows the configuration that resulted from ray tracing with various lenses. Figure 5.8-B shows the adapted configuration in which one new lens was added to create more space between the beam splitter and the filter wheel of the spectrometer.

A)

B)
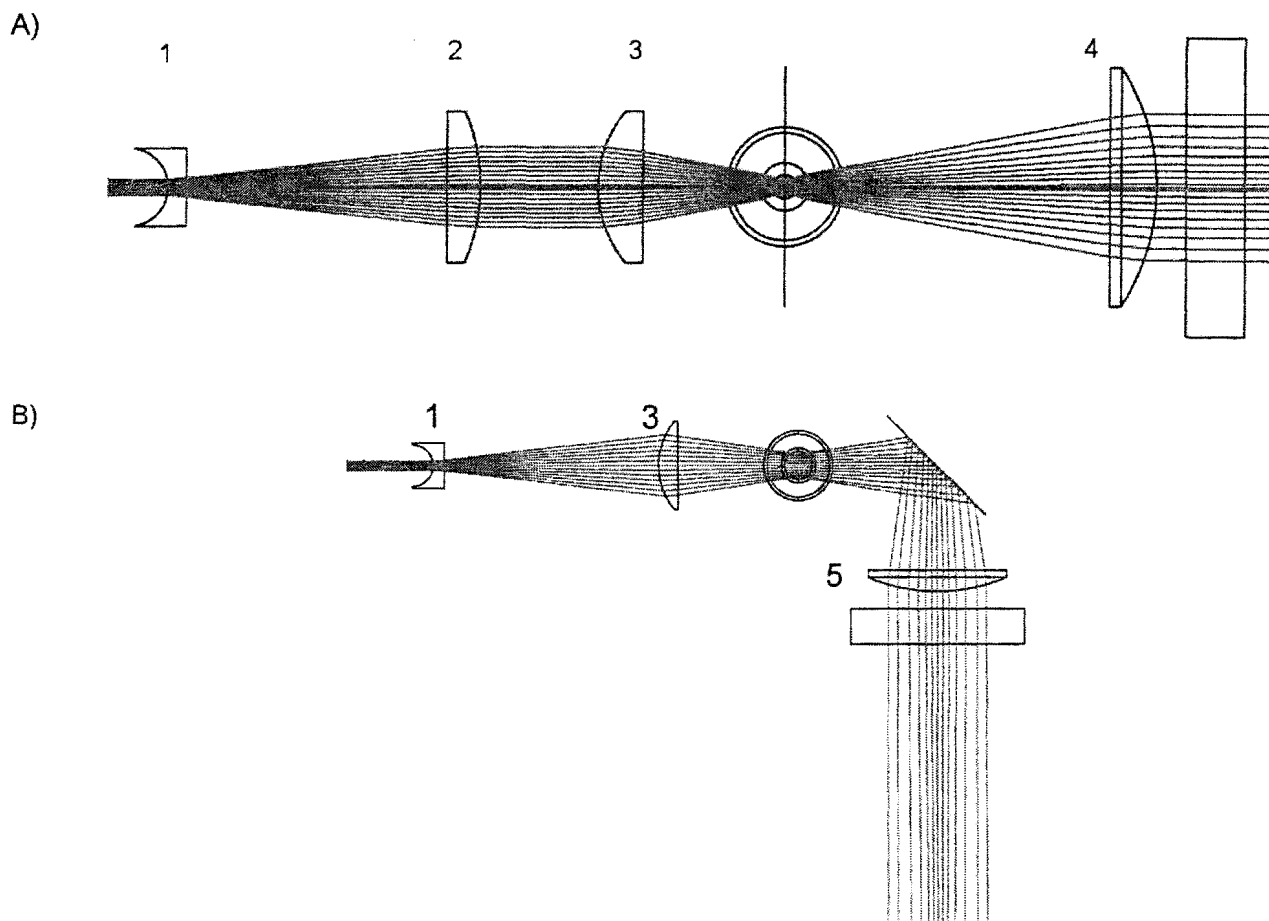
Figure 5.8 Schematics of the optical designs for the 4mm inner diameter burner design, which was used for testing and the optical design for the 8mm inner diameter burner used in the parabolic flights.

In both configurations the problem with the high exit angle and the collimation through the interference filter are solved and standard cylindrical lenses can be used. Even the beam path through the burner is such that no calibrations or corrections will be required for the Abel-inversion.

Figure 5.9-A shows the ray trace results for the transmission through the 8 mm quartz burner. The graph in the figure shows how the lateral positions in the burner and the detectors are coupled, which makes calibration for data processing unneeded.

Furthermore in both configurations up to 90% of the burner diameter can be measured, which is higher than any of the previous optical configurations. Thus by incorporating the burner designs as an optical component, a compact design based on standard components has been found with which it is shown that lateral measurements are possible in HID-lamps without the need for moving detector or laser system.

For both lens systems the used lenses were anti-reflection coated, details of each of the lenses are listed in table 5.2.

A)   B)
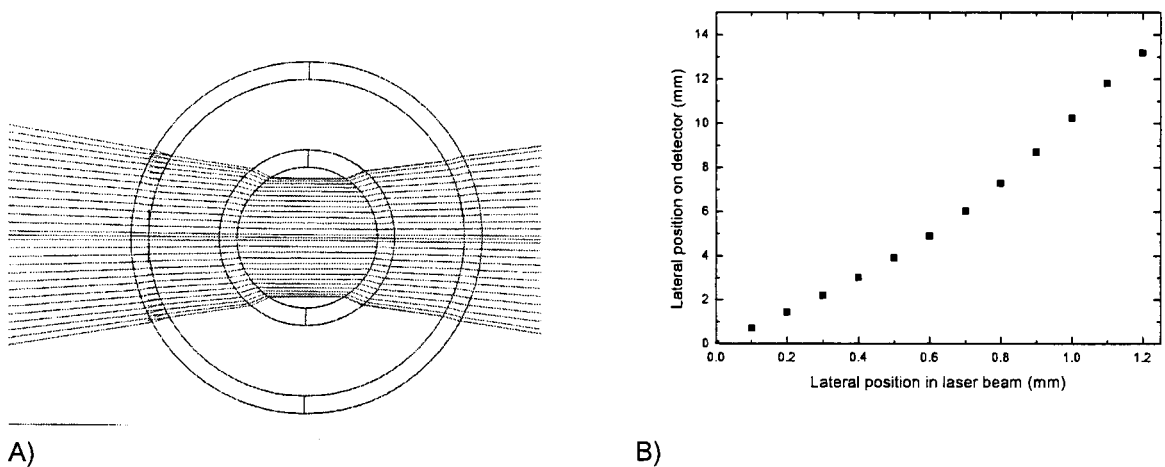
Figure 5.9 Ray trace result for the 8 mm burner and the correlation between lateral position in the burner and the position on the detector

Table 5.2 Specifications of the lenses used in the optical designs for both burner types

Lens	Company	Product Nr	Focal length	Type	Material	Coating
1	Melles Griot	01 LCN 001	-12.7 +/- 2%	Plano Concave Cylinder	BK7	078
2	Newport	CKX062	62.9 +/- 2%	Plano Convex Cylinder	BK7	AR.14
3	Newport	CKX038	38.1 +/- 2%	Plano Convex Cylinder	BK7	AR.14
4	Melles Griot	01 LPX 139	70 +/- 2%	Plano Convex Spherical	BK7	078
5	Melles Griot	01 LPX 179	100 +/- 2%	Plano Convex Spherical	BK7	078

5.4 Data acquisition and control system

For the setup a data acquisition and control system has been developed by the BLN group of the faculty of applied physics at Eindhoven University of technology. Initially one system would be developed to control all systems and data acquisition, however due to the little time available before the parabolic flight and the absence of a weight limit on the zero-g airplane it was chosen to incorporate the control systems of the laser diode system in the TU/e DACS sytem.

The data acquisition and control system TU/e DACS including the MLD 1000 controller of the diode laser system can be schematically seen as depicted in figure 5.10
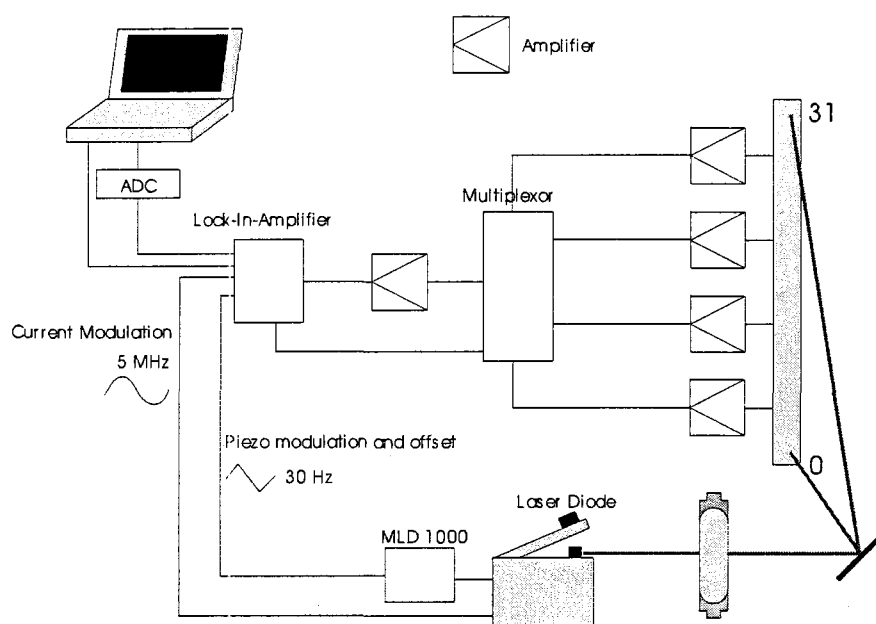
Figure 5.10 Schematic of the data acquisition system, with all the major components and wiring

First we will describe the data acquisition part of the system. The data acquisition starts with the signal generated by the photodiode array, on which the laser light that passed through the burner is imaged.

The analogue signal generated by each photo diode is preamplified and fed to the multiplexer. The multiplexer acts as a switch board and selects from which photodiode the signal will be measured and passed through to the sampling circuits. The signal of the selected photodiode is again amplified before going to the lock-in amplifier chip.

The lock-in amplifier chip can be used in high frequency modulation with which up to a modulation frequency of 5 MHz can be detected. The signal that is generate by the lock-in procedure is then sampled by the Parallel sampling ADC unit (ParSam), from which the digitised data can be read with the software and either saved to disk or visualised on screen. For the data acquisition and control of the system a software package has been developed which gives full remote control of the settings of the laser system and handles the data acquisition automatically.

Previously it was described how the wavelength tuning of the laser system with the Piezo element can be done by applying an analogue signal with a certain DC offset voltage and a modulated signal on top of it to the analogue input on the Piezo amplifier. This option was used to obtain remote control of the laser system. The TU/e DACS control system is capable of generating a DC signal from -1 to 10 Volts with a saw-tooth modulation signal on top of it with a 16 bits DAC. The DC offset signal and the amplitude of the saw-tooth modulation signal can be set separately in the software.

The frequency of the saw-tooth modulation signal is fixed to 30 Hz, due to limitations of the ParSam unit. For the chosen 2000 samples per period of the Piezo modulation signal, 30

Hz was the highest obtainable Piezo modulation frequency, for the fastest sampling rate of the ParSam.

The control system of TU/e DACS handles the generation of the Piezo modulation signal, the clock signal for the multiplexer, the 5 MHz current modulation signal and triggering signal of the ParSam. All signals are generated from a central 10 MHz clock, which makes timing of all the events in the hardware possible.

The software package controls the multiplexer, the generation of the Piezo offset signal and saw-tooth modulation signal and retrieves the data collected on the ParSam. For the Piezo modulation signal, the rise time, the amplitude and delay time to prevent resonance effects on the Piezo element at the peaks of the modulation signal can be set in the software.

When operational, the software can be put into two different modes; oscilloscope mode and data acquisition mode. In oscilloscope mode the signal measured on one photodiode is continuously plotted to the screen of the laptop, with which a 30 Hz refresh rate of the signal on the selected photodiode is obtained. In this mode the operator can change the settings of the Piezo offset voltage and Piezo modulation amplitude and see the effects on the screen immediately. By adjusting both parameters the absorption profile can be found and centred on the flanks of the Piezo modulation signal. Also mode hops can be observed and the temperature of the system can be adjusted until a mode hop free region is found in which the full line profile can be measured. When the settings are satisfactory, the software can be switched to data acquisition mode or when during operations the settings need adjustment the software can be switched into oscilloscope mode. In figure 5.11 a screen shot of the used software in oscilloscope mode is given to give the reader and future operators an idea of the described options.
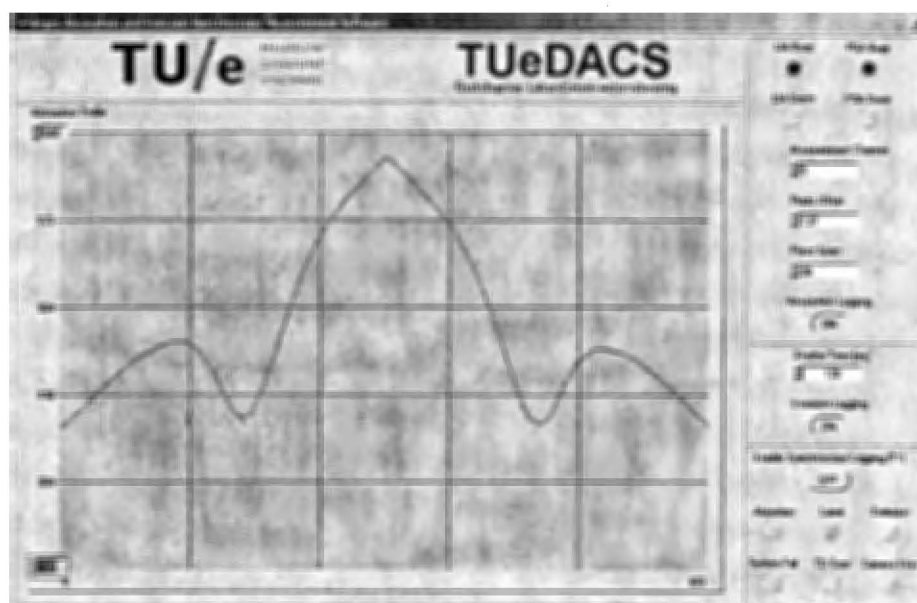

Figure 5.11 Screenshot of the data acquisition and control software in oscilloscope mode, during the measurement of a Dysprosium lamp burning at 150 W. The Piezo modulation saw-tooth signal with the absorption profile can be seen.

In data acquisition mode the software automatically selects each photodiode in the array by controlling the multiplexer and stores the sampled signals to disk. For each of the diodes the signal is sampled for one full period of the Piezo modulation signal and at 30 Hz roughly one second is needed to measure all 32 photodiodes. After a full array scan, the signal measured on the in the software selected photodiode is plotted to screen. Therefore roughly a 1 Hz refresh rate of the measured signal is seen in data acquisition mode, which is still sufficient to determine if the software settings need adjustment.

During the parabolic flights the software also switched the laser on and off, which was needed to measure the background emission signal of the lamps and switch the laser off when the CCD-camera was operational. The reason that the laser system had to be switched of is because the laser absorption setup and spectrometer measure in the same volume by using a beam-splitter and therefore 50% of the laser signal travels through the beam splitter and is imaged onto the entrance slit of the spectrometer. Measuring in the same volume has the advantage that the data resulting from both diagnostics are from the same position in the lamps and that the output of the laser system can be monitored with the spectrometer, but required timing of both measurement systems. Therefore the absorption measurements and emission measurements were alternated and every 3 measurements the laser system was switched of during a full array scan to obtain a background measurement.

6 Measurement techniques

6.1 Direct absorption technique

The tunable diode laser absorption spectroscopy technique (TDLAS) has proven to be an easy and direct way to measure particle densities in many applications. The same technique can be used with a tunable external cavity diode laser system and is called external cavity tunable diode laser absorption spectroscopy (EC-TDLAS).
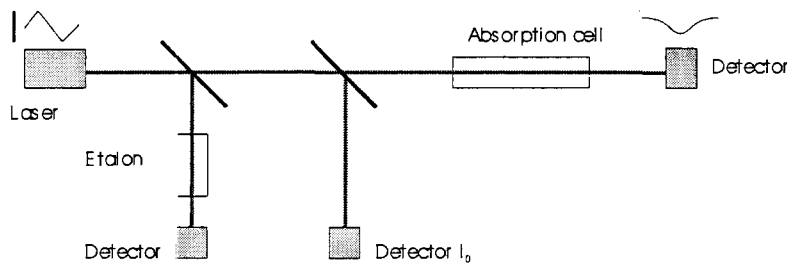

Figure 6.1 schematic of a typical TDLAS setup

The laser wavelength is tuned and the transmitted intensity is measured with a detector. From the Lambert-beer law, equation 2.5, it is apparent that not the transmitted intensity, but I/I_0 is the quantity of interest. Therefore the laser intensity before the absorption in the cell, I_0, must be known. Often I_0 is measured with a beam splitter and an extra detector, the wavelength tuning is often monitored with an etalon by measuring the transmittance through the etalon with a third detector, see figure 6.1. In our application the available space and weight limit the size and complexity of the setup and preferably no extra detectors and optical components were added to the setup.

When a diode laser is tuned by changing the current, the intensity of the output changes accordingly. Therefore, in TDLAS I_0 can also be determined by fitting the data measured on the detector with a linear baseline function, by using the data far away from the absorption line profile where there is no absorption. This requires a large wavelength tuning range and linear intensity output of the laser system with the wavelength tuning.

However in an ECDL system the tuning is achieved by changing the position of the tuning mirror or grating with a Piezo element. The output intensity of the system is in this case not necessarily linear with the tuning of the wavelength as it would be with current tuning of the laser wavelength, since the output is determined by the transmission of the external cavity.

When operated over large tuning ranges the output intensity of the external cavity system changes in a non-linear way. Figure 6.2 shows the output of the laser diode when scanned over the full Piezo tuning range, in which multiple mode hops are visible as jumps in the output power.

During the measurements only a fraction of the full Piezo range is scanned, i.e. between two mode hops. As can be seen in the figure, the output is not linear between all the mode hops. It must be noted that the resolution of the measurement is poor. Although the Piezo wavelength tuning is linear for some regions within the Piezo tuning range, the baseline fitting procedure will not be a widely applicable procedure, which will result in problems when measuring multiple species by using the coarse tuning capability of the laser system or when the external cavity is realigned. Both the coarse tuning option and the realignment were needed and will be described in chapter 7 and are therefore already taken into account in this chapter and another way had to be found to determine I_0.
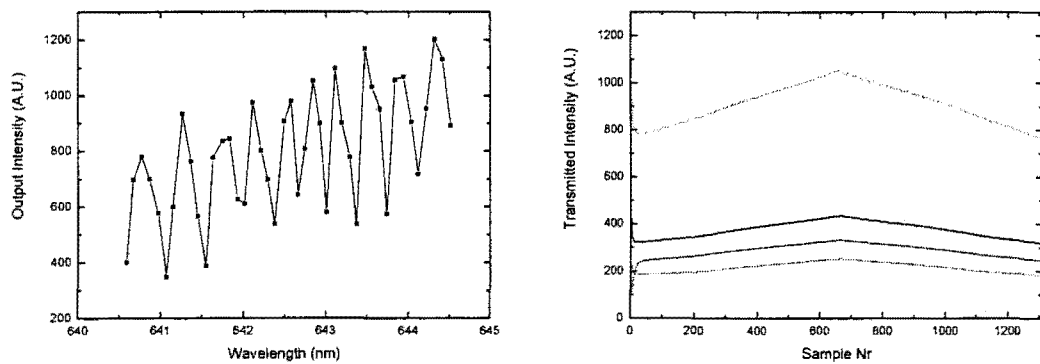
Figure 6.2 Left: Typical output of the external cavity diode laser system without current coupling. Right: The output of the laser system with current coupling for the maximum mode hop free tuning range of 0,.071 nm.

A second option to determine I_0 would be to measure a reference signal through the lamps before the lamps are ignited. However, measurements have shown that the transmission of the burner material changes and that the mechanical positioning of the burner in the BuBa, i.e. the metal suspension, changes due to the high temperature changes when the lamps are ignited. Therefore the reference signal method did not yield reliable results and could not be used.

A third option is the result of the option to couple the current fed to the diode to the applied Piezo voltage on the MLD 1000 controller unit. In this way the intensity output of the laser system is linear with the Piezo tuning. To demonstrate the effect of the current coupling, 4 channels of a measurement with a lamp switched off and the current coupling activated are pictured in the right graph of figure 6.2. The effect of the current coupling effect, as can be seen in right figure of figure 6.2, is clearly linear. The vibrations on the signal are caused by other set-ups in the zero-g airplane and people walking around.

Another feature that might be noted by the reader is the starting output intensity of the photodiodes, which is caused by the capacitive working of the photodiodes. The diodes are charged when the multiplexer is set to another photodiode and they discharge when selected for measurement, as can be seen in the figure as the steep fall of the measured intensity in the first 20 samples.

With the current coupling the reference intensity I_0 can be determined in a very compact way from the measurement and furthermore the absorption feature can be found easier on a linear changing background than on a fluctuating background. This is very convenient in adjusting the Piezo offset being weightless in the ISS or during the parabolic flight, where the human actions must be as simple and as little as possible due to the high stress levels on the body and the likeliness of illness during the parabolic flights.

6.2 Baseline fitting procedure

In the previous section we have stated that by coupling the laser current to the Piezo voltage, the reference signal can be obtained from the measured absorption signal. Figure 6.3-A shows the result of a measurement in a Cerium Iodide lamp operated at 150 W.
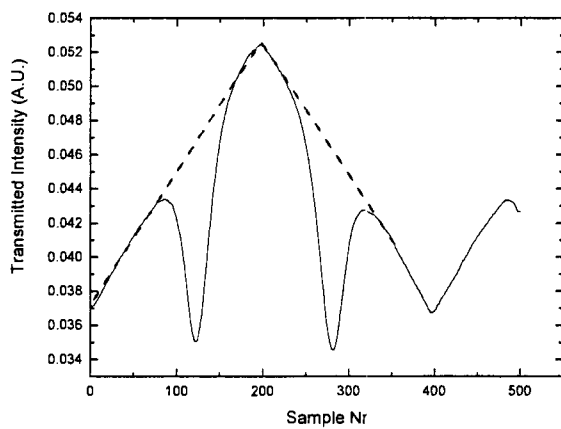
A) Measurement in a Cerium-Iodide lamp at 150W
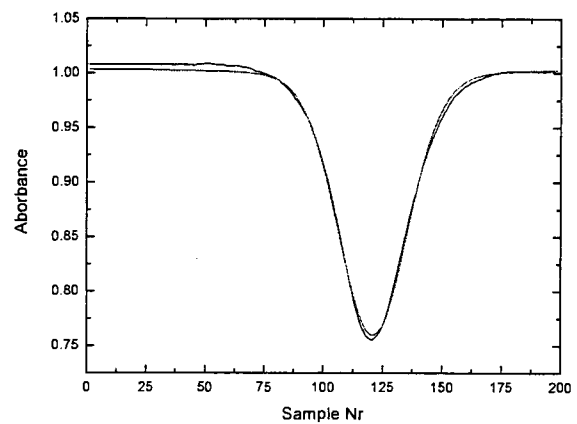
B) Result after averaging and correcting with the fitted baseline. The result has been fitted with a Voigt function

Figure 6.3 Example of a measured absorption signal with current coupling, base line fitting procedure and the resulting lateral absorbance

The modulation of the Piezo voltage with the saw tooth-signal and the influence of the current coupling on the intensity of the laser are clearly visible in the measurement. The signal was measured for 1,5 periods of the Piezo modulation signal. On the ascending flank the system tunes to higher wavelengths and on the descending flank the system tunes to lower wavelengths. The data acquisition system has been designed to measure one full period of the Piezo modulation signal on each detector in the array, in that way obtaining 2 absorption features per channel per scan.

By mirroring one of the 2 features and matching the minima of the profiles and averaging the result, irregularities caused by vibrations and hysterese are suppressed. By fitting the mirrored and averaged measurement with a linear function the baseline, I_0, was found.

The Absorbance was found by dividing the measured data with the data obtained from the base line fitting. Figure 6.3-B shows the resulting absorbance after mirroring, averaging and dividing by the fitted reference intensity I_0. The result has been fitted with a Voigt profile to show that the fitting procedure is successful on the measured data. It must be noted that the Voigt profile is symmetric and as can be seen in the figure the fit is slightly off at the left side of the profile. This is caused by a slight error in the first derivative of the fitted baseline.

6.3 Wavelength modulation spectroscopy

The intensity differences origination from the absorption were expected to be much smaller than the intensity output of the laser system and a very small signal would have to be measured on a very large background signal.

To improve the detection limits of TDLAS systems, often modulation techniques in combination with a lock-in amplifier are utilised. Considering the time available for testing and the fact the HID-lamps designed for the parabolic flights became available in the week before the parabolic flight campaign, it was decided to adapt the system for high frequency wavelength modulation to be on the safe side. A lock-in chip capable of detecting modulation signals up to 5 MHz was selected and added to the design of the TU/e DACS system.

In wavelength modulation spectroscopy often a high frequency periodic signal is added on the tuning signal of the system, which in TDLAS is the laser diode current. The modulated current results in a small change in wavelength and is therefore tuned at a high frequency around the output wavelength of the laser system. In the schematic below is depicted how the small change in output wavelength results in a change in the transmitted intensity. The change in transmitted intensity has obviously the same frequency as the modulation signal and the amplitude of the signal is proportional to the first derivative of the absorption feature for a modulation amplitude much smaller than the line width of the profile and therefore wavelength modulation spectroscopy is often called derivative spectroscopy. In the figures below, the effect of the modulation signal and the a typical first derivative output of a lock-in are depicted.
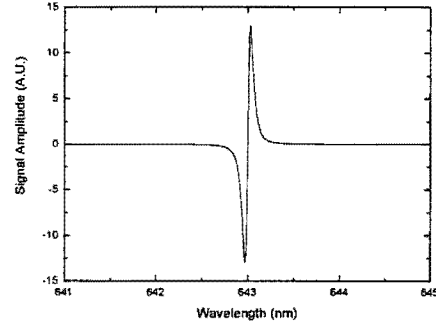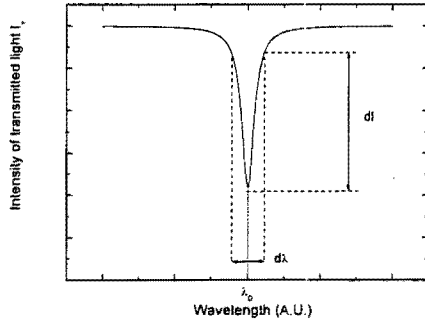
To apply the same technique in the ECDL system, the laser head was modified and a bias-T module was added to the electronics. With the Bias-T module a high frequency signal between 10 kHz and 10 MHz can be added onto the current supplied to the laser diode by the MLD-1000 controller.

To see the influence of the Piezo wavelength tuning, the current coupling and the amplitude modulation induced by the current modulation on the output of the lock-in amplifier the output of the lock-in was derived including all the signals and effects of the ECDL system. The laser diode current is written as the sum of the current supplied by the MLD-1000 controller and the modulation signal applied to the Bias-T module:

$$i_{ic}(t) = i_c + i_a \cos(2\pi f t) \tag{6.1}$$

The resulting wavelength modulation and amplitude modulation can be written as:

$$v(t) = \upsilon_c + \upsilon_a \cos(2\pi f t) \tag{6.2}$$

and

$$I_L(t) = c_{cpr}(i(t) - i_{th}) = c_{cpr}(i_c + i_a \cos(2\pi f t) - i_{th}) \tag{6.3}$$

The output of the lock-in resulting from the modulation signals and absorption of the signals described by the Lambert-beer law was derived, a detailed description of the derivation is given in appendix B:

$$O_{lock-in} = \frac{1}{2} i_a c_{cpr} - \frac{1}{2} C_{cpr}(i_c - i_{th}) \frac{d\alpha(\upsilon)}{d\upsilon}\bigg|_{\upsilon=\upsilon_c} + \frac{1}{2} i_a C_{cpr}\alpha(\upsilon) + \frac{3}{32}\upsilon_a^{\,2} \frac{d^2\alpha(\upsilon)}{d\upsilon^2}\bigg|_{\upsilon=\upsilon_v} \tag{6.4}$$

It is clear that the output contains the first derivative of the line profile $\alpha(v)$. It also shows that the other terms, which are the result of the intensity modulation induced by the current

modulation often called Residual Amplitude Modulation (RAM), influence the output of the lock-in.

One can imagine that the intensity variation caused by the wavelength modulation is much smaller for broader line profiles than for very thin line profiles, i.e. the first derivative of the profile gives small values. However the intensity modulation induced by the current modulation has the same value and in our situation is so strong that the first derivative signal is lost in the RAM signal.

To correct for the RAM signal, a reference signal was measured similar to as depicted in figure 6.2-B, both signals were subtracted or divided before passing into the lock-in amplifier. From these measurements a derivative signal could be obtained.

However the current-coupling characteristics change over the laser sheet, i.e. the intensity change with the wavelength tuning is different for each channel. This can be seen in figure 6.2-B as the changing first derivative for different channels of the measured intensity for the modulation of the current coupled Piezo wavelength tuning. To obtain the correct reference signal for each of the channels an identical photodiode array, lamp and optical system would be needed.

Therefore, when the first measurements showed that absorption signals up to 40% were measured, which made it possible to measure without the lock-in chip, it was decided not to use the lock-in technique in the space version of the setup to gain time and manpower.

7 Calibration and characteristics of the laser system

7.1 Laser diode operating temperature

In section 3 it was stated that laser diodes are very temperature dependent and that temperature stability is important for the stability of the output of the diode. There are 3 parameters that change with the temperature of the diode laser system; threshold current, output wavelength and lifetime. The lifetime of a laser diode is increased at lower operating temperatures at a typical rate that with a decrease of 10 degrees the lifetime is doubled. The threshold current of the laser diode increases with increasing temperature; hence the maximum achievable output power decreases with increasing temperature, because the maximum value of the laser current does not change with temperature.

We have seen that the requirements of the system for use in the international space station are very demanding. Due to the limited cooling power, the environmental temperature inside the dome structure will be around 40 degrees. The manufacturer set the operating temperature of the laser diode at 22.0 °C. Thus the Peltier element used to stabilize the temperature of the diode laser has to cool the laser over a temperature difference of 18 °C. The maximum cooling power of the Peltier element is 16 Watts, which is not sufficient enough to maintain the 22 degrees Celsius of the laser diode, the external cavity and cooling block. Therefore the laser diode must operate at a higher temperature.

To test the capabilities of the laser diode in the sys500 system, the output power of the laser for different set laser currents and different temperatures was measured. During the measurements the Piezo voltage was fixed at 50.0 Volt. Every 30 minutes an output power-current characteristic was measured.
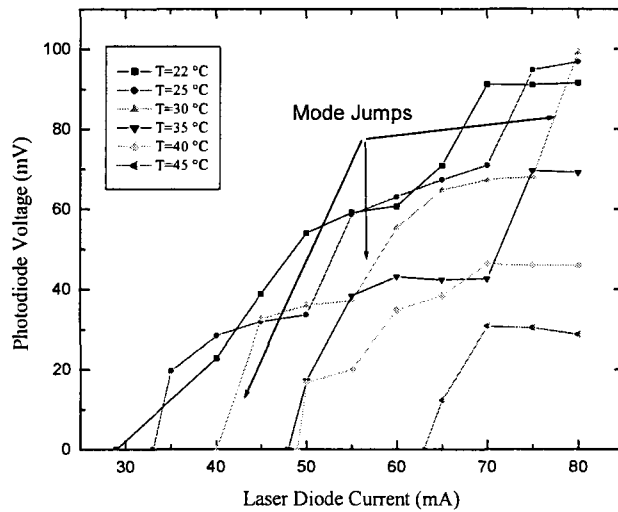
Figure 7.1 Output power-current characteristic of the sys-500 sn:575 system for different set temperatures of the temperature control unit

From figure 7.1 it is apparent that with increasing temperatures the threshold current of the laser diode increases and that the maximum output power of the laser diode decreases. At 40 degrees the output power is still more than 50% of the maximum power.

Another feature of the graphs are the typical hops in output power. For example the line T=25 °C shows 3 jumps in the output power, which are caused by mode hopping. The figure also shows that with increasing temperature the mode hops shift to higher currents. This is the reason why the laser system can obtain any wavelength in the tuning range. By changing the temperature, the mode structure can be moved and with the external cavity any wavelength can be selected.

From the measurements it follows that the laser can be operated in an environmental temperature between 30 and 50 degrees Celsius, because with the cooling capacity of the Peltier element a temperature difference of 10 degrees with the environment can be maintained.

7.2 Calibration of the Piezo offset and Piezo span

Often the wavelength tuning of a laser system is monitored by an etalon from which the transmission can be related to an absolute wavelenght value, which in our setup is virtually impossible due to the limited available space. Therefore the correlation between the set Piezo span, Piezo offset and output wavelength had to be calibrated.

There are a number of parameters that can be set on the controller and in the software of the TU/e DACS system that determine the output of the system; laser current, Piezo offset voltage, Piezo span voltage, the cavity temperature and the Piezo offset on the Piezo amplifier unit.

The Piezo modulation span and offset are generated by the TU/e DACS system and the generated analog signal is fed to the Piezo amplifier unit of the MLD-1000 controller. The generated signal is amplified in the amplifier and added to the set value on the controller itself. When using the system it is important to set the values on the controller to a fixed value and control the offset with the software to be able to use the calibration measurements.

The Piezo offset signal generated by TU/e DACS can be set between 0-10 Volts with a stepsize of 39 mV. The Piezo modulation span can be set between 0 and 7 Volt with a step size of 27 mV. Typical values for Piezo span and offset are 50.0 Volt and 700 mV respectively.

To calibrate the output of the system, the Piezo offset on the amplifier was set to its minimum value and the voltage generated by the amplifier was recorded for different software settings. The software can be set to an integer number between 0 and 254. The result is given in figure 7.2
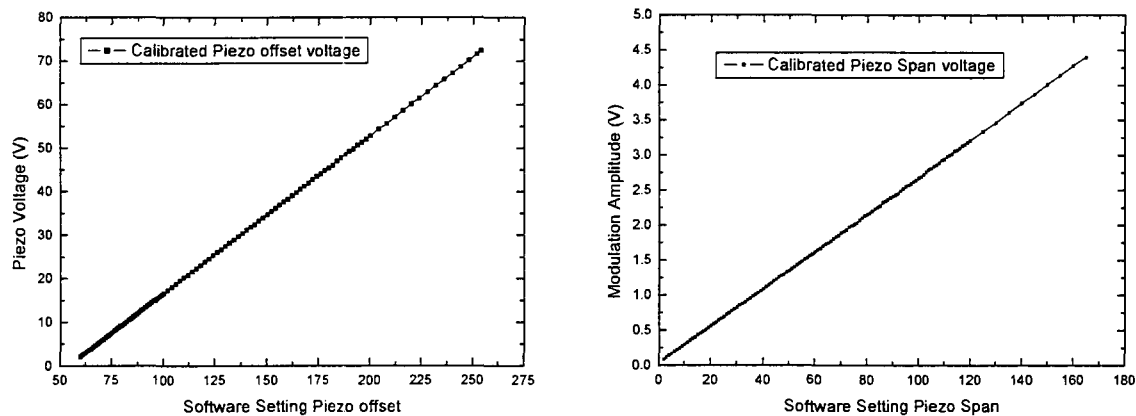
Figure 7.2 Calibration of the Piezo offset and Piezo span generated by the TU/e-DACS system

In a similar way the Piezo modulation span amplitude was measured with an oscilloscope and the result is given in right graph of figure 7.2. With both calibrations, the absolute voltages applied to the Piezo element and the modulation amplitude of the Piezo voltage are known.

To relate the voltage applied to the Piezo element to the emitted wavelength two procedures were used. In the first procedure, used in the laboratory, the output of the laser was monitored with a 1-m monochromator on a CCD camera. To calibrate the monochromator and SBIG-CCD camera a spectrum of a 150 W Cerium-Iodide lamp was taken, with which the pixels could be absolutely calibrated to the wavelength by locating known emission lines in the Kurucz database [7] and finding the position of the lines in the CCD images.

When the absorption components were adapted and built into the setup, calibration in the laboratory became difficult because the system would have to be taken apart completely for calibration of the laser absorption setup. Each time the calibration would have to be repeated

when the laser system had been re-aligned or after changing a damaged laser diode, which unfortunately happened 2 times during tests due to EMI from the ignition pulses of the lamp electronics.

In the second procedure the built in spectrometer was used. Figures 5.2 and 5.3 showed that the laser sheet is reflected with a beam splitter onto the detector. However, the light transmitted trough the beam splitter enters the imaging system of the spectrometer situated in front of the entrance slit of the spectrometer. By adjusting the axial position of the laser sheet, the transmitted light was imaged on the entrance slit of the spectrometer and the wavelength could be monitored on the built in CCD camera.

Calibration of the laser system and coarse tuning to the absorption lines of the other species could then be easily performed by following the laser light with the spectrometer. The spectrometer system was calibrated from a cerium spectrum taken from a lamp burning at 150 W. Figure 7.3 shows a measured cerium spectrum and the emission lines selected from the Kurucz database that were used for calibration.
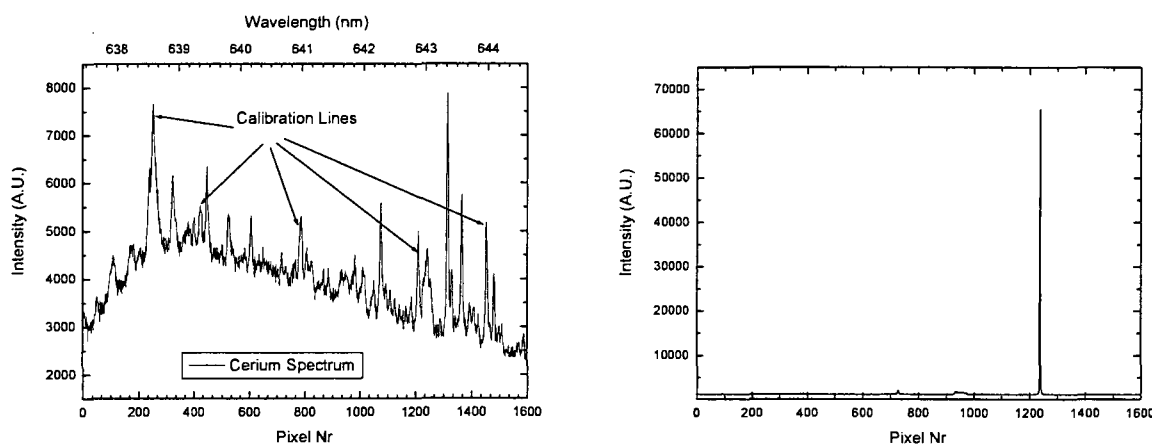
Figure 7.3 Left: Spectrum taken with the spectrometer for calibration of the laser system with the selected emission lines used for the wavelength calibration. Right: Spectrum of the output of the laser, taken with the spectrometer

7.3 Piezo Tuning range of the external cavity

In sections 3 and 5.1 it was described that the external cavity diode laser can be tuned by rotating the mirror with a Piezo element. The Piezo element mounted under the mirror can be extended or shortened by applying a voltage over the element. To determine the wavelength-tuning characteristic of the external cavity, the output wavelength was measured as a function of the set Piezo offset voltage. The output wavelength was measured using a 1-m monochromator and an SBIG-ST6 CCD-camera. The results are plotted in figure 7.4.
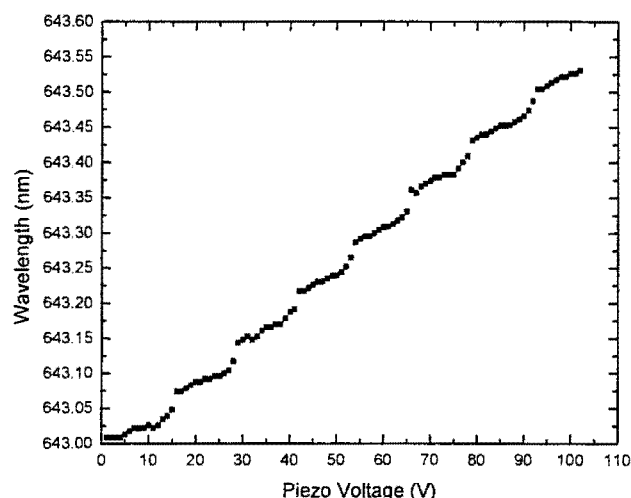
Figure 7.4 Piezo driven wavelength-tuning characteristic of the TEC-500 laser system

From the measurement it follows that the full Piezo tuning range is as specified 0.5 nm and that the mode hop free tuning range without current coupling is 0.04 nm. The measurement also shows the mode structure of the diode laser. The limited resolution of the monochromator and the used software to locate the maximum of the laser line profile on the CCD images sometimes resulted in the non linear tuning behavior between mode hops due to saturation of the CCD camera. Note that the mode structure is not fixed in wavelength due to the coarse tuning capability of the system and the temperature behavior of the laser diode with temperature.

7.4 Coarse Tuning and element selection

At first the system would be used to study the Cerium-Iodide additive in the HID-lamps as was listed in the requirements in chapter 4. During the building period and testing of the system in the laboratory it became important to measure other salt additives, like scandium- and dysprosium-iodide. In this section the possibility of multiple element selection are explored.

To perform absorption measurements on other elements, optically thin resonant or near-resonant lines for those elements are needed which are optically thick enough to result in a measurable absorption signal, but still are optically thin enough to validate the Taylor-expansion of the Lambert-Beer law. Furthermore the lines need to be within the tuning range of the diode laser.

From the selection procedure in chapter 4, lines were found in the vicinity of the already selected Cerium 643.4388 nm line.

Cerium	643.4388 nm
Scandium	641.3430 nm

Dysprosium	642.1913 nm

We have seen that the maximum wavelength tuning range with the Piezo element is 0.5 nm. Although the lines are relatively close to the cerium line, the Piezo tuning range is not sufficient to tune to the other selected lines from the cerium line at 643.4388 nm.

In the TEC-500 system the Piezo element is clamped between a positioning screw and the rotating mirror. By turning the screw the laser output wavelength can be tuned over a much larger range. This is called coarse tuning of the laser system. The specifications of the manufacturer indicate a coarse tuning range of 10 nm and a wavelength change of 5 nm per revolution.
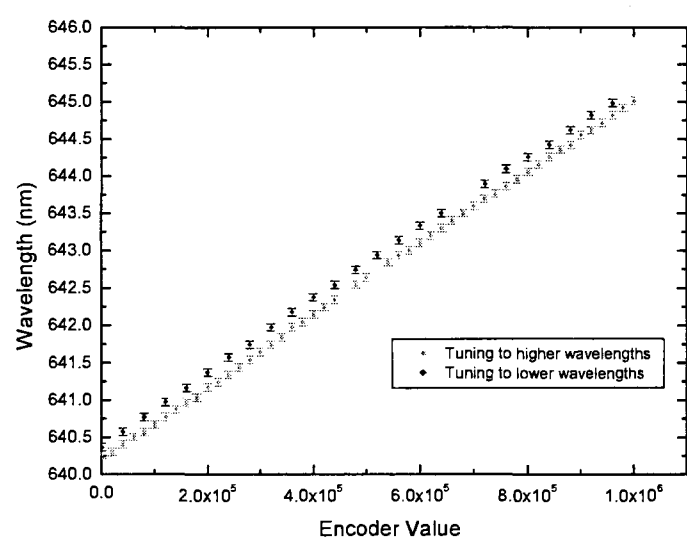
Figure 7.5 Calibration of the coarse wavelength tuning of the diode laser system with the Maxon motor steering and controller software.

To be able to remotely adjust the laser wavelength with the coarse tuning screw, the laser head was adapted and equipped with a Maxon stepper motor. The rotation of the stepper motor axis is monitored with an encoder to be able to absolutely position the motor and keep it fixed at the set position.

Using the 1-m monochromator, the coarse tuning range of the Maxon motor steering was calibrated and the result is given in figure 7.5. The figure shows that the three selected lines for the elements can be obtained with coarse tuning of the laser system with the Maxon motor steering. The encoder on the motor makes it possible to obtain very high relative accuracy and with 1 million counts per revolution a resolution of 5 10^{-6} nm/count can be achieved with a feed-back control system.

Note the difference in output wavelength when tuning to higher or lower wavelengths. This is caused by play on the flexible connection between the motor and the drive shaft and should be taken into account when coarse tuning the system.

7.5 Preliminary in-house vibration test

To test the individual system components before the official vibration testing to reveal as many problems before the setup would be build together, a 1-dimension vibration testing setup was built by G.C.S. Schiffelers [23]. With the system small components up to 2 kg can be tested. The construction of the mirror mount and the special design lever to translate and rotate the mirror of the laser system around its pivot pount seemed like a fragile construction. Furthermore the Piezo element is clamped between the lever construction and the coarse tuning screw by a strong spring. Therefore it was expected that the laser diode system as it is delivered off the shelve would need to be modified. And therefore the laser head, without the bottom cooling plate, was tested first and subjected to the by ESA specified forces for the Progress launch and its entering into trajectory to the international space station.

The specified vibrational forces are for two different types of test; random constructed vibrations to mimic the vibrations during launch and slowly frequency tuned vibrations to test for resonance effects. The table below lists the settings derived from the specifications.

Frequency range (Hz)	Amplitude (g)	Time (min)
5-25	1	1
25-200	1-3	2
200-800	3-5	3
800-1500	5-8	4
1500-2500	8	5

The laser head was subjected to the specified forces. At the time the forces and resonances could not yet be measured with the g-force meter, but the resonances could be heard very clearly by listening to the sound generated by the system. The the laser diode head, with a Piezo element clamped in, survived multiple tests without any damage. From these preliminary tests it is clear that the unmodified design, even with 2 resonaces in the system, complies with the specifications and that the ECDL-system, althouh some modifications might be need, can be succesfully launched into space.

8 Measurement results

During the design and manufacturing of the total setup for the parabolic flights, the diode laser system and TU/e DACS system were tested in a temporary laboratory setup with HID-lamps used for experiments in Kitt-peak [20]. For the measurements in the parabolic flight campaing a different lamp design was used to maximize the segregration effects. In this chapter the first preliminary results of the parabolic flight campaign and the results obtained from the KITT-peak lamps will be presented and compared. Furthermore the influence of the used burner design will be shown.

8.1 Absorption measurements in micro-gravity and hyper gravity

To test the setup and the chosen lamp configurations, salt fillings and burner design, measurements in micro-gravity conditions were performed in the 34st parabolic flight campaign of ESA, carried out by Novespace. During the 3-day campaign each day 31 parabolic flights, as schematically depicted in figure 8.1-A, were made with an airbus 300 airplane. During each parabola everything in the airplane is subjected to micro-gravity for a period of 20 seconds, i.e. everything becomes weightless for 20 seconds. During a micro-gravity phase the gravitational forces in all directions are less than 0.01 g.
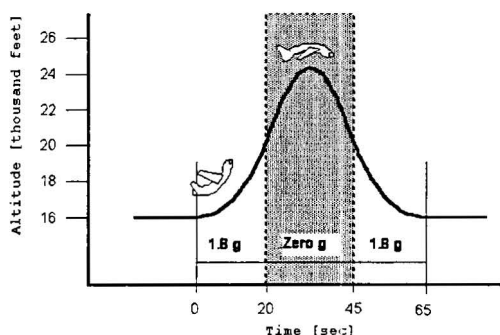
A) Duration times of the different gravity phases during one parabola

B) The airbus 300 zero-g airplane

Figure 8.1 Graph of the parabolic path flown by the zero-g airbus 300 airplane and the zero-g airplane.

During the first two days, measurements were performed on quartz burners to study the segregation effects. On the third day lamps with PCA-burners were observed to study the effects of micro gravity on the helical instabilities. 20 Lamps were fitted into the carousel, of which 13 lamps were made with quartz burners with either cerium or dysprosium as salt additives. For each additive a range of mercury doses were chosen. Table 8.1 lists the used type of lamps, their fillings and at which day they were measured.

Table 8.1 Overview of the various lamp parameters

Carrousel position	Salt Additive	Mercury Dosage	Day of Measurement
1	CeI_3	10mg	2
2	CeI_3	10mg	2
3	CeI_3	10mg	-
4	CeI_3	7 mg	2
5	CeI_3	7 mg	2
6	CeI_3	7 mg	-
7	DyI_3	10 mg	-
8	DyI_3	10 mg	1,2
9	DyI_3	10 mg	1
10	DyI_3	7 mg	1
11	DyI_3	7 mg	1,2
12	DyI_3	3 mg	1
20	DyI_3	5mg	1

8.2 The effects of the burner design on the line profiles

In the laboratory lamps with an inner diameter of 4 mm were successfully measured with a Piezo tuning range of 0.04 nm. Since the requirements were based on these lamps, the settings in the software were fixed at the values used in the laboratory.

However, when the first 8 mm lamps were lighted at the airport in Bordeaux no absorption signal could be found. After realigning the laser system on the spot, the Piezo tuning range could be increased to 0.071 nm and the absorption feature of the dysprosium lamps appeared.

After calibrating the setup again, to ensure that the set tuning ranges were right, it was clear that the line profiles of the 8 mm lamps were much broader than in the 4 mm burner lamps. The effect of the line broadening was to such extend that the cerium line, which has a much smaller transition probability than the selected dysprosium line, could no longer be measured for low power settings. Only at the maximum power of 150 Watt, the absorption profile could be measured.

The mercury fillings of these lamps were chosen in such way that the mercury pressure in the 4 mm designs should be comparable to the 8 mm designs with a mercury dosage of 3 mg. Taken into account that it was expected that the dominating line broadening would be mainly Van Der Waals broadening by the mercury buffer gas, similar line widths are expected for comparable mercury pressures. To show the difference in line widths, the measured lateral

profile line widths were fitted with a Lorentzian profile and the resulting line widths are listed for 3 different lamps in table 8.2.

Table 8.2 Line widths measured in a 4 mm burner design and 8 mm burner design

Salt Additive	Mercury dose	Power (W)	Line width (nm)	Burner Design
CeI_3	0.75 mg	150	0.002	4mm
DyI_3	0.75 mg	150	0.0058	4mm
DyI_3	3 mg	150	0.016	8mm

M. Haverlag measured line widths of typically 0.001 nm for cerium lamps using a Fourier spectrometer in Kitt-peak [20]. Two of the Kitt-peak lamps were used for testing in the laboratory and for these lamps a line width of 0.002 nm was measured for the Cerium lamp and 0.0058 nm for the Dysprosium lamp. However, the measurements from the parabolic flight campaign resulted for a dysprosium lamp with an 8 mm inner diameter burner in a line width of 0.016 nm. Which is almost the tripled value of the line widths measured in the laboratory. The difference in the broadening can be caused by 3 different effects; The laser line width was much broader after realignment of the system, the mercury dosage of one of the type of lamps was different than specified or the mercury distribution throughout the burner was different due to a contracted temperature profile.

Laser profile line width

At first an explanation was sought in the characteristics of the laser system, because the measured absorption profiles are a convolution of the laser line profile with the absorption line profile and the precise profile of the laser was not known after realigning the system on the airport in Bordeaux.

To test if the laser line profile was broadened, the experiments with the 4 mm lamps were repeated in the setup used in the parabolic flights. These measurements resulted in the line widths that were measured in the laboratory before the parabolic flight campaign and are given in the table above. With the laser line profile line width ruled out as an explanation, the only other variable remaining that could affect the line broadening is the buffer gas, i.e. the mercury density.

Mercury dosage

If the mercury density would be much higher the theory of pressure broadening, the line profile would become broader. The method used at Philips to determine the amount of mercury put into the burner has proven to be a stable and relatively straightforward technique over the years and it is therefore very unlikely that the specified dosages are not correct. For now it is assumed that the mercury dosages in the lamps were as specified, until the chemical

analysis of the lamps performed at Philips Central Development Lamps is completed and proves otherwise.

Contracted temperature profile

In a fully equilibrated discharge, the mercury pressure is constant throughout the burner and the local temperature determines the local mercury density. In a fully developed discharge the temperature profile is often assumed parabolic [21]. Figure 8.2-A shows a typical parabolic temperature profile for a HID lamp, with the corresponding mercury distribution. It shows that the mercury density is high at the colder burner walls and low in the middle of the lamps.
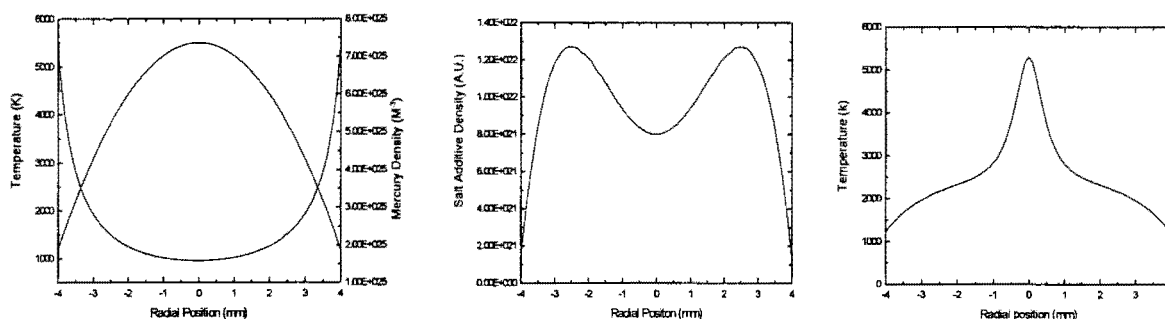
Figure 8.2 Graphs of A) a parabolic temperature profile and the corresponding mercury density B) A typieal hollow density profile of the salt additives C) A contracted temperature profile

At the walls where the temperature is typically around 1200 K only salt molecules exist, i.e. DyI_3. The molecules are dissociated in the discharge into dysprosium atoms and iodide:

$$DyI_3 \rightarrow Dy + I_3$$
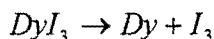
Together with the radial segregation this results in a hollow density profile of the salt atoms as is depicted in figure 8.2-B.

These figures show that where the mercury density is high, the salt additive density is low. Because the line widths of the lateral measured profiles are mostly determined by the region where both densities are the highest, the difference in line broadening can be explained with a different mercury distribution. If the mercury density would increase in the regions where the peaks in the density of the hollow profile are, the measured lateral line profiles would become broader.

As stated earlier, the mercury density is determined by the temperature profile in the lamp and changes for a different temperature profile. If a contracted temperature profile is assumed, as is depicted in figure 8.2-c, the mercury density will become higher where the additive density is high, i.e. at the plateaus of the temperature profile, and the line profiles will become broader. At the time of writing this report the temperature profiles were not exactly known, but preliminary results calculated from the emission measurements using Boltzmann

plots by G.C.S. Schiffelers, indicate a contracted temperature profile [23]. The results of the calculations are given in figure 8.3 and although the temperature values are not absolute values, the relative values clearly show that the temperature profiles are contracted.
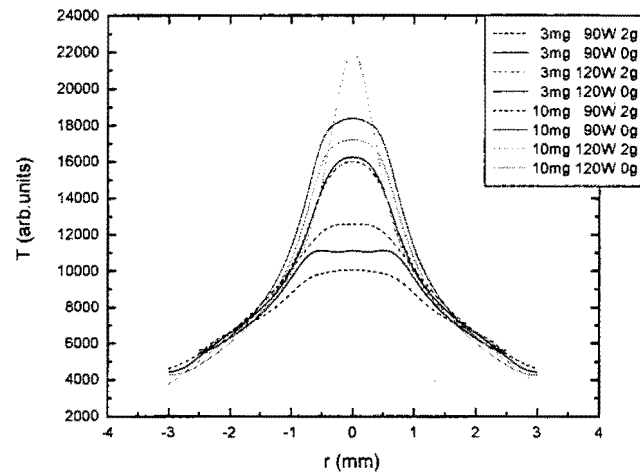
Figure 8.3 Calculated temperature profiles from Boltzmann plots constructed from the emission measurements performed in the parabolic flight campaign, for various lamps and gravity conditions

Furthermore models have shown that for certain lamp configurations the temperature profile is not fully developed and that the temperature profile is contracted [24] [25]. From the experiments, the indications given by the models and the Boltzmann plots, it follows that the temperature profile is a contracted profile. With which the 8 mm lamps contain a hot center and a three times larger cold plasma volume than the 4 mm lamps. In these colder regions there is roughly three times more mercury present, from which the broader lines result.

8.3 Effect of the limited mode hop free tuning range

The downside of the broader line profiles is that the line profile wings cannot be measured completely due to the limited mode hop free tuning range of the diode laser system. The system specifications indicate a mode hop free tuning range of 0.04 nm without current coupling and of the 3 bought laser systems, the best diode was capable of reaching a tuning range of 0.071 nm with current coupling.

Even with the for this type of laser diode large tuning range, the flanks of the line profiles could not be obtained. Since the accuracy of the measurement, and therefore the resulting density, is highly dependent on how accurate the baseline can be reconstructed on the flanks of the lateral measurements this is a serious limitation of the laser system on the type of lamps that can be measured.

To show the effect of the line broadening effect on the measured data, two measurements of dysprosium lamps burning at 120 W and different mercury doses are plotted in figure 8.4.
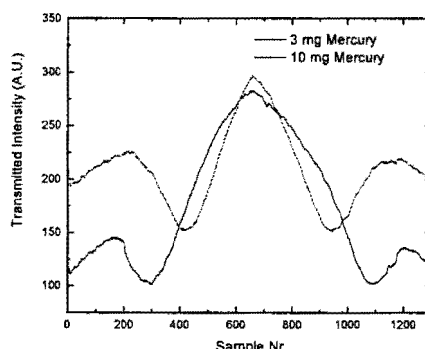
Figure 8.4 Measured lateral profiles for two mercury dosages and a power setting of 120 Watt

As expected with pressure broadening, the line profile width is larger for the lamp with the higher mercury dosage. The graph also shows that even with the lowest mercury dosage of 3 mg the line profile is already too broad to obtain an accurate baseline. For the 10 mg lamp, the maximum output power of the laser system is never reached because top of the actual Piezo modulated laser output signal is absorbed by the absorption profile and only one flank remains with which the reference intensity can be reconstructed.

By extrapolating the measured data in principle the absorption line profile and the reference intensity can be reconstructed. Due to the inaccurate reference intensity and the vibrations of the airplane and neighboring setups, the quality of the resulting data is not high enough to obtain density values accurate enough to obtain sensible density profiles from the Abel-inversion procedure. This is even more important in Abel-inversion for different wavelengths to reconstruct the absorption line profiles radially, which is necessary when the absorption profile line width varies over the radial position, which is the case as we will see in paragraph 8.8. Therefore only trends can be visualized and no absolute density profiles were obtained.

8.4 Measurements in Micro gravity and hyper gravity

Before the plane enters the micro gravity phase, the airplane has to make a steep climb (pull-up) until a 47 degree angle between the planes trajectory and the horizon is reached, see figure 8.1-B. After the micro-gravity phase a similar manoevre is made to level the airplane from the 47 degrees diving angle (pull-out). During the pull-up and pull-out everything in the airplane is subject to a force of two times the normal gravity force. The force is always directed downward as if the airplane were flying horizontal.

Therefore during a sequence of parabolas the equipment is subjected for one minute to a force of 1-g, followed by 20 seconds of 2-g, then the 20 seconds of microgravity and after the

20 seconds of 2-g during the pull-out the cycle is repeated. The cycle gives the opportunity to observe the lamps under various gravity conditions. To study the behaviour of the lamps with power, the power was increased at the beginning of each cycle with 15 Watts and each lamp was burned at 5 different powers from 75-150 Watts.

Effect of the lamp power setting

In figure 8.4 the raw measurement data of lamp nr 9 are plotted for the three gravity phases and for 3 power steps to show the influence of the gravitational forces. Before ignition the additive-salt is present in a condensed form. When after ignition the temperature reaches a certain value, the salt starts to evaporate and the evaporated molecules are dissociated in the discharge. During operating an equilibrium exists between the evaporation of molecules from the salt pool and condensation of the salt molecules to the salt pool. Therefore the additves are not measurable untill the temperature reaches the threshold at a specific power setting.

This treshold effect of the power setting is clearly seen in all the three gravity phases, where below a power setting of 90 Watts for all phases of the parabola no absorption signal is measured.
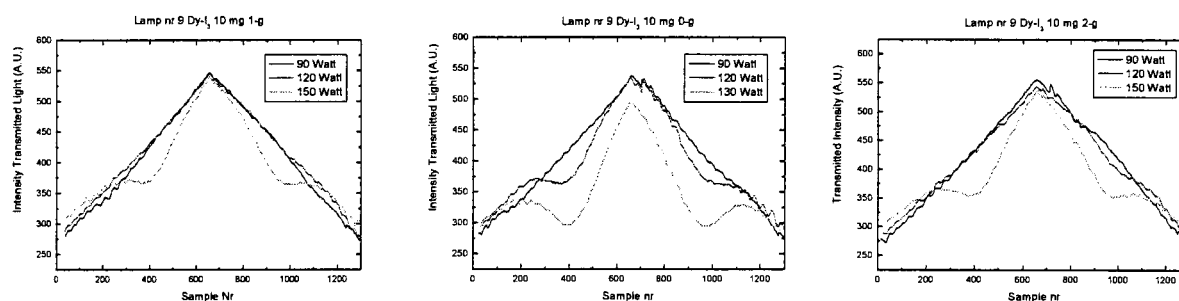
Figure 8.5 Measurements of lamp nr 9 in the 3 gravity phase of a parabolic sequence for 3 different lamp powers

The laser sheet is passing through the middle part of the burner and when the axial demixing, as described in section 1.2, is in such the cerium or dysprosium atoms are either below or above the measurement volume, no signal will be measured. With increasing power, more molecules will evaporate and therefore more atoms will be in the plasma, i.e. the overall density increases. With each power step the amount of additive atoms increases untill it reaches a measurable or stronger value in the measurement volume, which can be seen clearly in all graphs.

Effect of the gravitational forces

During the micro gravity phase the gravity forces are no longer sustaining the convectional flows and therefore the axial demixing is reversed and the discharge starts to mix in axial

direction. The mixing causes the additive atoms, which are either situated above or below the measurement volume, to enter the measurement volume and for the same power setting there will be more signal in the 0-g phase, or there will be signal for lower power settings than in the normal gravity phase.

In the 2-g phase the extra gravity forces induce more convection and it is expected that the discharge becomes more demixed. The measurement in figure 8.5-C shows that this is not the case, there is even more signal than for the same power setting in the 1-g phase. The stronger convectional flows in the 2-g phase of the parabola have a mixing effect in stead of the expected stronger demixing effect.

8.5 Measurements for different mercury doses

From the measured data a power scan for different mercury fillings was made. The results are plotted in the figures below. For the 3 mg lamp the data for the first two power steps were lost by setting a wrong Piezo offset value in the system.

The current limitation of the lamp power supply also limits the maximum applied power to the lamp for lower mercury doses. The mercury pressure in the lamps mainly determines the voltage over the lamps. Therefore if the lamp voltage drops below 75 Volt, the ballast cannot supply the lamp with 150 W due to its current limit (2 A) and therefore the power settings in the measurements of the 3 mg lamp had little or no effect.
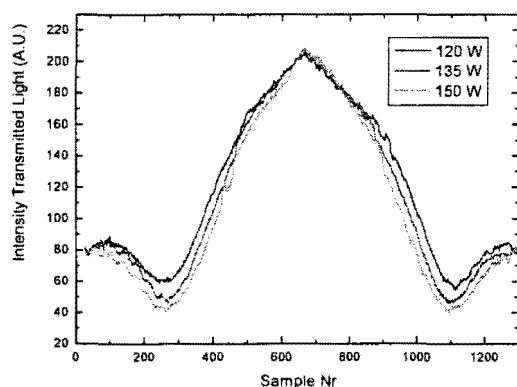
A) 3 mg
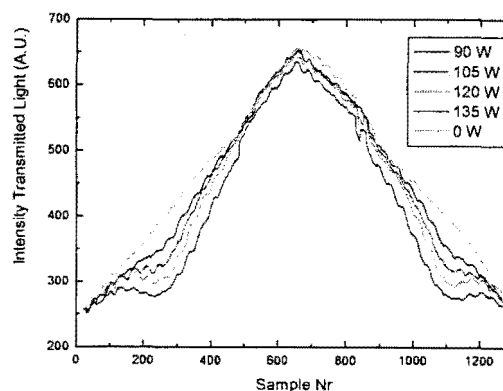
B) 5 mg

C) 7 mg   D) 10 mg

Figure 8.6 Measurement results from Dysprosium-Iodide lamps for different power settings and different mercury fillings measured at the end of the micro gravity period.

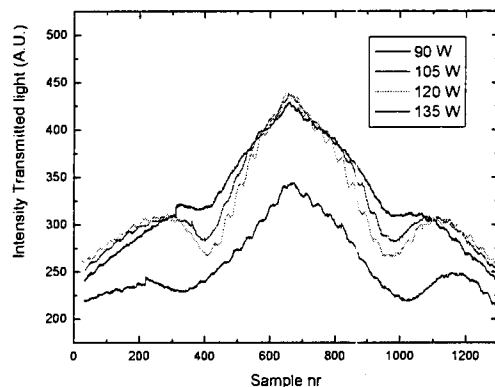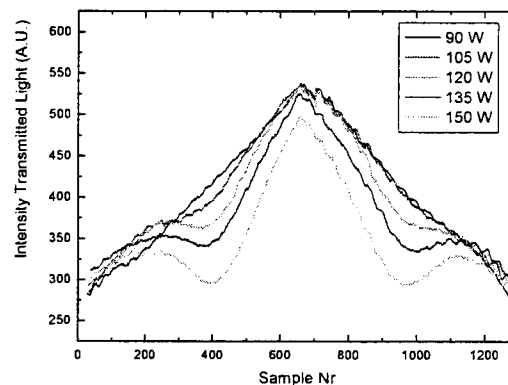The vibrations of the setup are clearly seen on the measurements from the other 3 lamps. The reason for the sensitivity of the measurements to vibrations is the suspension of the burner in the BuBa. Due to the high temperatures and temperature differences, the suspension must be able to handle the change in size of the metal contacts, which is achieved with a spring like construction. Therefore the construction is highly sensitive to vibrations, which can be seen in the measurements as wave-like changes in the transmitted intensity.

Again the problem that arises from the extra pressure broadening is clearly visible in figure 8.6-D, where the maximum measured intensity is lower for 150 W, than for the lower power settings. This is due to a broader than the tuning range of the laser system and the absorption line profile extends beyond the maximum, absorbing the top of the baseline signal. It is clear that the baseline fitting procedure will give inaccurate results for the highest power settings and that from these data no accurate density profiles can be obtained. The figures also indicate that density can be obtained from measurements in 3, 5 and for the first 3 power steps in a 7 mg lamp.

8.6 Time dependence of the measurements during micro-gravity

For the used lamps, the typical time to stabilize is in the order of minutes. Therefore the 20 seconds of micro gravity cannot result in a stable situation, which is one of the main reasons that the segregational effects can only be studied in the ISS.

The data acquisition system alternated the emission and absorption measurements. A full array scan with retrieving the data from the system could be finished within a second, for the emission system the needed time frame was 2 seconds. Therefore every 4 seconds a full array scan could be obtained from the laser absorption setup. To correct the measurement data for background emission, a background scan was made by turning the laser diode off in

one out of three measurements. In figure 8.7 the background corrected signals from one detector measured during one parabola are plotted. The parabola started at 11:07:25 and ended at 11:07:46.
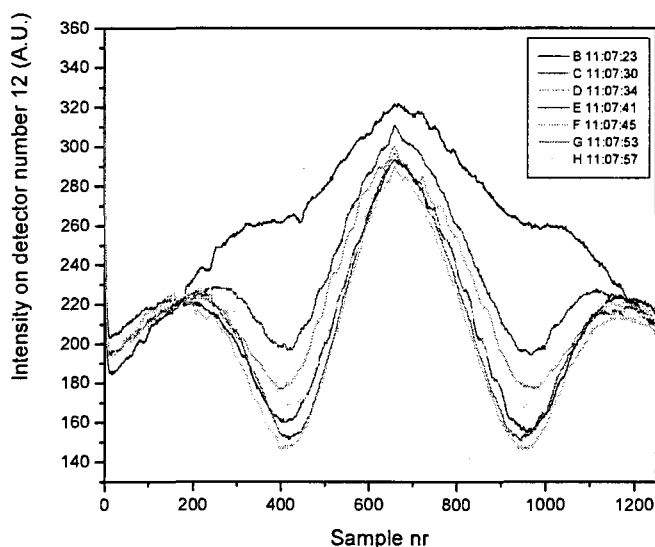
Figure 8.7 Measured profiles on detector nr 12, taken during a complete micro-gravity phase of the parabola

From the figure it is clear that that a stable situation is never reached, the measured profiles get stronger with the in axial mixing discharge. The demixing effect immediately starts when the parabolic maneuver is ended, as can be seen as the absorption signal getting weaker.

8.7 Lateral resolved absorbance

When the approximation of the Beer-Lamberts law is used and the lateral absorbance $(-\frac{I - I_0}{I_0})$, from equation 2.5, is plotted against the lateral position for the measured lateral profiles, the integral over the absorption coefficient is obtained. This integral is dependent on the density of the absorbing species, the wavelength and the absorption path length. By correcting for the absorption path length (line of sight) relative trends in the particle distributions are visualised.

Figure 8.8 shows the results of the corrected and calculated absorbance for a 5 mg dysprosium lamp burning at 120 Watt in the three gravity phases of a particular parabola and for a power setting of 150 Watt at the end of the micro-gravity phase.
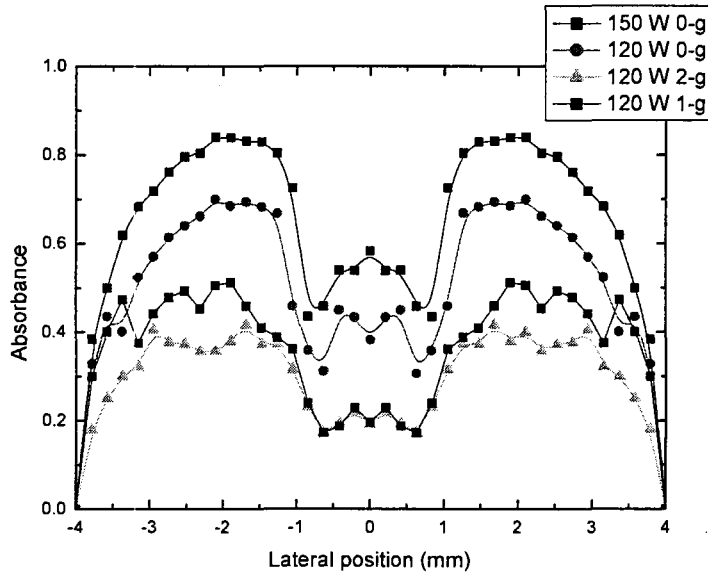
Figure 8.8 Calculated lateral absorbance for the different gravity phases and 2 power settings of the lamp power supply

Although the raw data had a lot of noise on it and smoothing and averaging of the data was used to obtain the absorbance values, trends are still visible. The earlier described and expected hollow profile is clearly visible and if the data were to be Abel-inverted an even more hollow profile would result from it.

The dip in the middle of the profile would become almost zero, which indicates that the relative amount of dysprosium is very low in that region of the discharge. The only reason for the steep flanks on the sides can be found in contraction of the discharge. In the discharge higher temperature induces two processes that cause depletion of dysprosium atoms; the dysprosium atoms are ionized due to the high gas temperature and the faster diffusion process of the dysprosium atoms is faster for higher temperatures. Considering the steep flanks of the dysprosium absorbance, the plasma discharge must be contracted, which is also indicated by the strongly contracted temperature profiles.

With higher power settings the overall dysprosium density increases. The difference in overall absorbance, i.e. the area under the curves, corresponds with the axial mixing effect during the micro gravity phase and the extra axial demixing in the 2-g phase of the parabola, meaning that the data are qualitatively understood.

An unexpected feature of the profiles is the small peak in the center. A hollow profile was expected due to the radial demixing effect. The peak means that in the center of the discharge where the temperature is the highest, a higher concentration of dysprosium atoms is present. This might be caused by the production of dysprosium neutrals by dissociation of dysprosium-Iodide molecules in the discharge.

8.8 Lateral absorbance profile line width scan

The goal of the micro gravity measurements is to obtain radial density information of the salt additives in the discharge. To go from lateral measurements to radial information, the lateral measurements have to be Abel-inverted. When the Abel-inversion is done directly on the integrated lateral profiles, the absorption line profile width must be constant over de radial position. Since the temperature profile is expected to be strongly contracted, also the width of the absorption profile is expected to change over the radius due do the varying mercury density.

For a full array scan, the lateral line profiles were obtained for each channel with the base line fitting procedure described in section 6.2. Each of the obtained line profiles has been fitted with a Lorentzian function and the line width of each of the profiles, resulting from the fits, were plotted in figure 8.9. As mentioned before the line broadening effect in the 8 mm burner made accurate reconstruction of the profiles almost impossible and hence the resulting line widths are the result of fitting on data with a lot of noise and inaccurate base lines and the result is merely plotted to show a trend in the line widths.
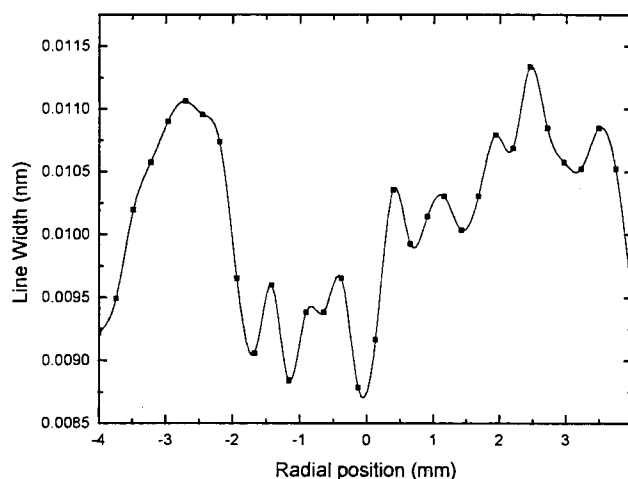
Figure 8.9 Line width variations in the lateral profile of a Dysprosium Iodide Lamp with an 8 mm burner diameter burning at 120 Watt

From the figure it can be seen that the line width of the profiles changes over the lateral position, which is another indication for the contracted temperature profile. It means that direct Abel-inversion of the measurements is not possible and that the Abel-inversion has to be performed per wavelength. From these results the line profile would be reconstructed and a radially resolved line profile would be obtained. From the integration of these reconstructed profiles the density of the absorbing species would then be obtained from equation 2.13.

9 Conclusions

From the performed measurements during the preparations for the parabolic flight campaign and the experiments performed in the parabolic flight campaign the following main conclusions were drawn:

Main conclusions

- A tunable diode laser absorption setup with the specified characteristics based on quartz lamps with an inner burner diameter of 4 mm was build and successfully tested in the 34th parabolic flight campaign of ESA. Absorption measurements were performed on HID-lamps with scandium, cerium and dysprosium as salt additives.

- The lateral absorbance profile for the dysprosium additive indicates that the plasma is strongly contracted and that in the future experiments on HID lamps are needed to select lamps

Detailed conclusions

- It was shown that tunable diode laser absorption spectroscopy is a direct and relatively easy way to study high-pressure discharge lamps with a very sturdy and stable design with the capability to operate in the international space station, which might also be interesting in other applications like a in production environment.

- A maximum wavelength tuning range of 0.071 nm could be achieved by coupling the current to the Piezo voltage and a range of 0.04 nm without current coupling with the Piezo modulation.

- Operation of the laser diode system with temperature stabilizing and data acquisition is achieved within the power budget specified for operation of the system in the International Space Station.

- Measurements with the laser absorption system can be performed up to 50 degrees Celsius of the laser system and a temperature difference of 10 degrees Celsius with the environment can be reached with the Peltier element in such way that the laser temperature is stabile at the set value.

- Coarse tuning of the tunable diode laser system was successful and each of the three salt additives, Cerium, Dysprosium and Scandium could be measured by adjusting the mirror position with a motor.

- By incorporating the burner designs into the optical system, designs for two different burner designs were made with which up to 90% of the burner diameter could be measured. The laser sheet passed through the burners with a nearly parallel beam and an exit angle of the laser sheet was achieved that made it possible to collimate the laser sheet through an interference filter onto a detector array.

- The baseline fitting procedure proved to be a simple and easy way to reconstruct the laser intensity profile and obtain an intensity reference.

- The results of the measurements show that 20 seconds of micro gravity is not long enough for the HID lamps to completely mix and reach a stable situation

- Laterally resolved and calculated absorbances show that the dysprosium distribution is as expected a hollow profile.

- The main line broadening effect is Van Der Waals broadening.

- Experiments in 8 mm burners with dysprosium show that the absorption profile line width varies over the radial position and that the Abel-inversion has to be done per wavelength to reconstruct the line profiles radially.

- High quality measurements in 8 mm burners with mercury doses above 5 mg are not possible due to extra Van Der Waals broadening caused by higher mercury densities in the outer regions of the burner and very accurate and absolute measurements would be needed to accurately reconstruct the thinner line profiles in the centre of the burner.

- A contracted temperature profile is the underlying reason for the broader absorption profiles observed during the 34th ESA parabolic flight campaign in quartz burners with an inner diameter of 8mm.

- For lamps with mercury dosages of 3 mg, the maximum current of the ballast limits the maximum set power to 120 Watt.

- High frequency wavelength modulation spectroscopy cannot be used in direct absorption spectroscopy for very broad line profiles due to the high Residual Amplitude Modulation signal that is generated compared to the first derivative signal of the absorption features.

- Modulation of the current with a 5 MHz sinusoidal signal is achievable with the BIAS-Tee module in the modified laser head.

- A full diode array scan is performed in 1 second and time resolved measurements were performed during the 34th parabolic flight campaign.

- Measurements show that vibrations are a strong source of noise on the measured signal and that the signal variations are mainly caused by the flexible spring-like mounting of the burners in the BuBa.

- Preliminary vibration tests have shown that the laser head is capable of surviving the vibration forces specified by the European Space Agency.

10 References

[1] M. Haverlag. Segregation of HID Lamps; A Literature Study, Philips Central Development Lamps, Rep. CDL 01/10030, 2001

[2] J.J.F. Geijtenbeek. The Origin of De-mixing, Philips Central Development Lamps, Rep. CDL 01/20125, 2001

[3] R.M. Mihalcea, D.S.Baer and R.K. Hanson, A diode-laser absorption sensor system for combustion emission measurements, *Meas. Sci. Technol.* 9:327-338, 1998

[4] Spectrophysics, 1974, A.P. Thorne. Chapman and Hall & Science Paperbacks, London

[5] G.R. Kirchoff and R. Bunsen. Cehmical analysis by spectrum-observation, Philos. Mag. 20:89-98, 1860

[6] Plasma Diagnostics, 1968, W. Lochte-Holtgreven, North-Holland publishing company, Amsterdam.

[7] The Kurucz Spectroscopic Database, http://cfa-www.harvard.edu/amdata//ampdata/kurucz23/sekur.html

[8] The NIST Atomic Spectra Database, http://physics.nist.gov

[9] J.A.C.Broekaert. Analytical Atomic Spectrometry with Flames and Plasmas, Wiley-VCH, 2001.

[10] L.P. Bakker. Plasma Control of the Emission Spectrum of Mercury-Noble-gas Discharges. PhD thesis, Eindhoven University of Technology, 2000. ISBN 90-386-1659-7

[11] K.A.H. van Leeuwen, Diodelaser systems, Coarse material Eindhoven University of Technology, Coarse 3P210, 2003

[12] Laser components www.lasercompoents.co.uk

[13] Sacher Lasertechnik GmbH http://www.sacher.de data sheets

[14] Newport corporation, http://www.newport.com/

[15] ILX Lightwave http://www.ilxlightwave.com/

[16] Profile GmbH, http://www.profile-optsys.com

[17] M. Haverlag. Spectroscopic methods for the relative measurement of densities of the atoms of sodium, dysprosium, praseodymium, scandium, calcium, thallium and cerium in HID lamps. Philips Central Development Lamps, Rep. CDL 01/20069, 2001

[18] E. Fischer, Axial segregation in metal halide lamps, J. Appl. Phys. **52**:3233, 1976

[19] S.I. Chou. Diode-Laser Absorption Spectroscopy of Hydrogen Halides for Semiconductor Plasma Process Diagnostics. PhD thesis, Stanford University, 2000

[20] M. Haverlag. Spectral measurements of HID lamps with Ce, Dy and Sc additives with a high resolution Fourier spectrometer performed in KITT-peak USA. Philips Central Development Lamps, unpublished report.

[21] R.J. Zollweg, J. Appl. Phys. Vol. **49**:1077, 1978

[22] Zemax development corporation, http://www.zemax.com

[23] G.C.S. Schiffelers, master thesis Eindhoven University of Technology, to be published, 2003

[24] K. Charrada, G. Zissis, M. Stambouli, A study of the convective flow as a function of external parameters in high-pressure mercury lamps, J. Phys. D: Appl. Phys. **29**:753-760, 1996

[25] S. Hashiguch, S. Mori, K. Tachibana, Numerical investigation of vertical mercury arc operationg at Varous Tube Radii, Jpn. J. Appl. Phys. Vol. **36**:6533-6539, 1997

[26] E.A.H. Timmermans, M.J. van de Sande and J.A.M. van der Mullen. Plasma Characterization of an Atmospheric Microwave Plasma Torch Using Diode Laser Absorption Studies of the Argon $4S^3P_2$ State.

[27] J.M. de Regt. Fundamentals of Inductively Coupled Argon Plasmas, PhD thesis, Eindhoven University of Technology,1996, ISBN 90-386-0237-5

[28] J.M de Regt, J.A.M. van der Mullen. A diode laser absorption study on a 100 MHz argon ICP, *J. Phys. D:Appl. Phys.* 29:2404-2412, 1996

[29] P. Werle et al. Near- and mid-infrared laser-optical sensors for gas analysis, *Optics and Lasers in Engineering* 37:101-114,2002

[30] Profile Optische Systeme GmbH, Basic Notes Laser Diodes, 2000

[31] A. Körber. A simple $\Delta\lambda$-method for measurements of element pressures illustrated by application examples to HID lamps. Philips PFL-Aachen, Rep. 1322/98, 1998

[32] E.F. Worden, J.G. Conway, B. Comaskey, J.A.D. Stockdale and F. Nehring. Determination of absolute transition probabilities in neutral cerium from branching ratio and lifetime measurements, *J. Opt. Soc. Am. B*, Vol. 8:1545-1558, 1991

[33] Laser Spectroscopy, 1996, Wolfgang Demtröder. Springer-Verlag Berlin Heidelberg New York. 2nd edition.

[34] Vertilas GmbH, specifications of Vertilas VCSEL laser diodes

[35] ILX lightwave Application note No. 8 Mode Hopping in Semiconductor Lasers

[36] ILX lightwave Application note No. 5 An Overview of Laser Diode Characteristics

[37] P. Kluczynski, J. Gustafsson, M. Lindberg and O. Axner, Wavelength modulation absorption spectrometry – an extensive scrutiny of the generation of signals, Spectrochimica Acta Part B **56**:1277, 2001

Appendix A. Abel inversion coefficients for fitting procedure

Approximated radial profile:

$$a(r) = \sum_0^n c_n r^n \tag{A.1}$$

Calculation of the lateral absorption values from the radial profile:

$$A(y,\lambda) = 2 \int_{r=y}^{\infty} \frac{a(r,\lambda)r}{\sqrt{r^2 - y^2}} dr = \int_{r=y}^{\sqrt{R^2 - y^2}} 2dy\, r \sum_0^n c_n r^n\, dr \tag{A.2}$$

Evaluation of equation 1 results in the following terms and relations for the fit-coefficients:

$n = 0$	$2c_0 \sqrt{R^2 - y^2}\, dy$
$n = 1$	$c_1 dy \left[\sqrt{R^2 y^2}\, R + y^2 \ln\left(\sqrt{R^2 - y^2}\right) - y^2 \ln(y) \right]$
$n = 2$	$2c_2 \sqrt{R^2 - y^2} \left(\frac{1}{3}R^2 + \frac{2}{3}y^2 \right)$
$n = 3$	$\frac{1}{2}c_3 dy \sqrt{R^2 - y^2} \left[R^3 + \frac{3}{2}y^2 R \right] + \frac{3}{4}c_3 dy y^4 \ln\left[\sqrt{R^2 - y^2} + R\right] - \frac{3}{4}c_3 dy y^4 \ln(y)$
$n = 4$	$2c_4 \sqrt{R^2 - y^2} \left[\frac{1}{5}R^4 + \frac{4}{15}R^2 y^2 + \frac{8}{15}y^4 \right] dy$
$n = 5$	$c_5 dy \sqrt{R^2 - y^2} \left[\frac{1}{3}R^5 + \frac{5}{12}y^2 R^3 + \frac{5}{8}y^4 R \right] + \frac{5}{8}c_5 dy y^6 \left[\ln\left(\sqrt{R^2 - y^2} + R\right) - \ln(y) \right]$
$n = 6$	$2c_6 \sqrt{R^2 - y^2} \left(\frac{1}{7}R^6 - \frac{6}{35}R^4 y^2 + \frac{8}{35}R^2 y^4 + \frac{16}{35}y^6 \right) dy$

Appendix B.   Derivation of the first harmonic output of the lock-in amplifier

The wavelength-modulation is easily obtained from modulation of the laser current. Described in the following form:

$$i_{ic}(t) = i_c + i_a \cos(2\pi ft) \tag{B.1}$$

The effect of this modulation is twofold. Not only the output wavelength is modulated, but also at the same time the laser intensity is modulated. For both effects the following expressions hold:

$$v(t) = \upsilon_c + \upsilon_a \cos(2\pi ft) \tag{B.2}$$

$$I_L(t) = c_{cpr}(i(t) - i_{th}) = c_{cpr}(i_c + i_a \cos(2\pi ft) - i_{th}) \tag{B.3}$$

From Lamberts-Beer law it followed that for small absorption values, the transmitted intensity can be written as:

$$I_T(\upsilon) = I_L(\upsilon)(1 - \alpha(\upsilon)) \tag{B.4}$$

The modulation of the current results in wavelength modulation and unwanted residual amplitude modulation called RAM. Therefore the output of the lock-in amplifier is not only determined by the wavelength-modulated part, but also by the RAM signal. And since the RAM signal introduces the noise of the laser intensity output it is unwanted. In most derivations this effect is considered but never reflected in the calculations. In the derivation given in this section the effect of the RAM-signal will be included in the input signal of the lock-in amplifier. Combining equation (B.2) and (B.4) and the formula for the output of the lock-in amplifier we obtain:

$$S_{lock-in} = \frac{1}{\tau} \int_0^\tau c_{cpr}(i_c + i_a \cos(2\pi ft) - i_{th})(1 - \alpha(\upsilon_c + v_a \cos(2\pi ft)))\cos(2\pi nft + \theta_n)dt \tag{B.5}$$

This integral can be split up into 4 separate integrals:

$$\frac{1}{\tau}\int_0^\tau c_{cpr}(i_c - i_{th})\cos(2\pi nft + \theta_n)dt \tag{B.6}$$

$$\frac{1}{\tau}\int_0^\tau c_{cpr}i_a \cos(2\pi ft)\cos(2\pi nft + \theta_n)dt \tag{B.7}$$

$$-\frac{1}{\tau}\int_0^\tau c_{cpr}i_a \cos(2\pi ft)\alpha(\upsilon_c + \upsilon_a \cos(2\pi ft))\cos(2\pi nft + \theta_n)dt \tag{B.8}$$

$$-\frac{1}{\tau}\int_0^\tau c_{cpr}(i_c - i_{th})\alpha(\upsilon_c + \upsilon_a \cos(2\pi ft))\cos(2\pi nft + \theta_n)dt \tag{B.9}$$

The first integral can be neglected, since the integration of the signal by the lock-in amplifier is over a large number of modulation periods ($\tau \gg \frac{1}{f}$). The result of the integral in equation B.7 is straightforward and the result for the in phase-component ($\theta_n=0$) of the output is only non-zero for $n=1$:

$$\frac{1}{2}i_a c_{cpr}$$

The result shows clearly that the RAM adds a constant offset to the output of the lock-in signal. The offset values are typically much larger than the signal of interest. Therefore the laser intensity noise will be introduced to the lock-in signal via the RAM signal.

To be able to calculate the other 2, the line shape function is Taylor expanded:

$$\alpha(\upsilon_c + \upsilon_a \cos(2\pi ft)) = \sum_{n=0}^{\infty} \frac{d\alpha^n(\upsilon)}{d\upsilon^n}\Bigg|_{\upsilon=\upsilon_c} \upsilon_a^n \cos^n(2\pi ft) \tag{B.10}$$

The $\cos^n(2\pi ft)$ terms can be written as an expansion of $\cos(2\pi kft)$ terms:

$$\cos^n(2\pi ft) = \frac{1}{2^{n-1}}\sum_{m=0}^{n/2}\left(1 - \frac{\delta_{m0}}{2}\right)\binom{n}{\frac{n}{2} - m}\cos(2\pi 2mft) \qquad \text{for n even} \tag{B.11}$$

$$\cos^n(2\pi ft) = \frac{1}{2^{n-1}} \sum_{m=0}^{(n-1)/2} \binom{n}{\frac{n-1}{2}-m} \cos(2\pi(2m+1)ft) \qquad \text{for n odd} \qquad (B.12)$$

Due to the orthogonality of the cosine functions, only the terms proportional to $\cos(2\pi ft)$ will contribute to the in-phase component of the n-th harmonic output of the lock-in amplifier. If we write down the first terms of the Taylor expansion and consider the first 3 orders.

$$\sum_{n=0}^{\infty} \frac{d\alpha^n(\upsilon)}{d\upsilon^{\wedge n}}\bigg|_{\upsilon=\upsilon_c} \upsilon_a^{\ n} \cos^n(2\pi ft) = \alpha(\upsilon_c) + \frac{d\alpha(\upsilon)}{d\upsilon}\bigg|_{\upsilon=\upsilon_c} \upsilon_a \cos(2\pi ft) + \frac{1}{2!}\frac{d\alpha^2(\upsilon)}{d\upsilon^{\wedge 2}}\bigg|_{\upsilon=\upsilon_c} \upsilon_a^{\ 2} \cos^2(2\pi ft) + \ldots\ldots$$

$$(B.13)$$

And use the series expansion of (equation B.11), the second order cosine term results in a constant term and a term proportional to $\cos(2\pi 2ft)$. The orthogonality of the cosine function will eliminate both terms and if we look at the first harmonic of the lock-in (n=1) the outcome of the integral in equation B.9 is:

$$-\frac{1}{2}C_{cpr}(i_c - i_{th})\frac{d\alpha(\upsilon)}{d\upsilon}\bigg|_{\upsilon=\upsilon_c} \qquad (B.14)$$

Which is directly proportional to the first derivative of the absorption profile function. The result of the integral in equation B.8 will include the effect of the RAM signal and in similar way the result can be written as:

$$\frac{1}{2}i_a C_{cpr}\alpha(\upsilon) + \frac{3}{32}\upsilon_a^{\ 2}\frac{d^2\alpha(\upsilon)}{d\upsilon^2}\bigg|_{\upsilon=\upsilon_v} \qquad (B.15)$$

And the RAM signal results again in an unwanted term in the output of the lock-in. To reduce the influence of the RAM signal and reduce the effect of the amplitude noise on the RAM signal, often the laser beam is split into two separate beams, where one of the beams passes through the measurement volume and the other through a path with the same geometry but without the absorbing species. By subtracting or dividing both signals the RAM signal can be eliminated.

Appendix C. Spectroscopic data of the used salt additives

Table C.1 Spectroscopic data for the used additives [kur], [Nis]

Element	Dysprosium	Cerium	Scandium
Atomic Number	66	58	21
Atomic Mass	162.5	140.116	44.96
Electronic Configuration	$(Xe)4f^{10}6S^2$	$(Xe)4f^15d^16s^2$	$(Ar)3d^1 4s^2$
Upper Energy Level of Absorption Line	1.930239 eV	1.954873 eV	1.953697 eV
J Value Upper Level	8.0	3.0	2.5
Lower Energy Level of Absorption Line	0 eV	0.028376 eV	0.020873 eV
J Value Lower Level	8.0	2.0	2.5
Transition wavelength	642.1913 nm	643.4388 nm	641.3324 nm
Transition Probability [s^{-1}]	$1.615 \ 10^5 \ s^{-1}$	$8.410 \ 10^5 \ s^{-1}$	$1.323 \ 10^5 \ s^{-1}$
Oscillator strength f []	$9.99 \ 10^{-4}$	$7.43 \ 10^{-4}$	$2.83 \ 10^{-3}$
Electronic configuration upper level	S6p *8	Fds2 *3F	3d4s2 2D
Electronic configuration lower level	6s2 5I	F2ds	S(3D)4p 4F
Ionistation Energy	6.82 eV	6.57 eV	6.56 eV

Table C.2 Calculated values for the partition sum Q(T) of various salt-additives and their ions

T (k)	Ce	Ce^+	Dy	Dy^+	Sc	Sc^+
2500	57.9	61.2	19.6	31.0	9.5	16.5
3000	76.0	82.1	21.1	33.8	9.7	17.8
3500	101.0	107.8	24.5	37.7	9.9	19.1
4000	126.0	133.5	27.9	41.7	10.4	20.3
4500	158.4	161.8	34.1	47.7	11.0	21.5
5000	190.9	190.2	40.3	53.7	11.9	22.8
5500	231.3	219.8	50.7	62.4	12.9	23.9
6000	271.6	249.5	61.0	71.0	14.2	25.1